



Relict landscape evolution and fault reactivation in the eastern Tian Shan: insights from the Harlik Mountains

Zihao Zhao¹, Tianyi Shen², Guocan Wang^{1,2}, Peter van der Beek³, Yabo Zhou⁴, and Cheng Ma²

¹Institute of Geological Survey, China University of Geosciences, Wuhan, 430074, China

²Center for Global Tectonics, School of Earth Sciences, China University of Geosciences, Wuhan, 430074, China

³Institute of Geosciences, University of Potsdam, 14476 Potsdam, Germany

⁴PowerChina Huadong Engineering Corporation Limited, Hangzhou, 310012, China

Correspondence: Tianyi Shen (shenty@cug.edu.cn) and Guocan Wang (wgcan@cug.edu.cn)

Received: 24 November 2024 – Discussion started: 17 December 2024

Revised: 23 March 2025 – Accepted: 28 March 2025 – Published: 23 June 2025

Abstract. Relict low-relief surfaces, formed during tectonically quiescent periods and later modified by factors such as increased tectonic activity, are prevalent within the active mountain ranges of central Asia. However, their formation, preservation, and subsequent evolution within the Mesozoic–Cenozoic tectonic framework remain poorly understood. This study examines the low-relief surfaces of the Harlik Mountains, located in the easternmost Tian Shan, integrating digital terrain analysis, fluvial geomorphic analysis, structural geology, and low-temperature thermochronology to reconstruct their long-term geomorphic evolution. Our results reveal that these surfaces are segmented by WNW–ESE-striking faults, which initially experienced right-lateral transtensional movement followed by left-lateral strike-slip reactivation. Apatite fission-track (AFT) thermochronology of samples from relict surfaces yields AFT ages ranging from ~ 110 to ~ 100 Ma, while samples from fault zones record ages of 90–70 Ma. Thermal modeling of these samples indicates a period of moderate cooling in the mid- to late Early Cretaceous, followed by a prolonged slow cooling phase for the relict surfaces. In contrast, fault zones show rapid cooling during the 90–70 Ma interval. By integrating these results with previous findings, we propose that the mid- to late Early Cretaceous (~ 110 –100 Ma) cooling event corresponds to extensional collapse following building of the Mongol–Okhotsk orogen. This process, coupled with increased humidity, enhanced erosion, and relief reduction, facilitated the formation of low-relief surfaces. The influence of Mongol–Okhotsk orogenic collapse likely persisted into the Late Cretaceous (90–70 Ma), during which right-

lateral transtensional faulting further segmented the landscape without generating significant topographic contrasts. By the Oligocene (~ 30 Ma), far-field effects from the India–Eurasia collision reactivated major faults in a left-lateral sense, driving regional uplift, surface tilting, and drainage incision. This uplift phase marked the end of landscape stability, as evidenced by increased sediment input into adjacent basins. Despite active faulting and fluvial incision, generally low erosion rates allowed the preservation of large-scale Mesozoic low-relief surfaces.

1 Introduction

In orogenic belts worldwide, extensive high-elevation, low-relief surfaces, typically forming summit plateaus or terraced pediments, bear testament to long-standing interactions between tectonic and surface processes (Phillips, 2002; Calvet et al., 2015; Whipple et al., 2017). Erosion rates drop considerably with decreasing topography, leading to the formation of low-relief surfaces, whose preservation is influenced by both tectonic stability and climatic conditions (e.g., van der Beek et al., 2009; Rohrmann et al., 2012; Morin et al., 2019). However, the processes behind their origin, preservation, and later modification remain a significant topic of debate. In particular, there is continued uncertainty regarding whether these low-relief surfaces developed at lower elevations and were subsequently uplifted during a phase of tectonic activity (Clark et al., 2006; Hetzel et al., 2011; Jaiswara et al., 2019) or whether they initially formed at high eleva-

tions within a tectonically uplifted environment (Liu-Zeng et al., 2008; van der Beek et al., 2009; Rohrmann et al., 2012; Cao et al., 2018). The distinction between these scenarios is challenging because it relies on differentiating surface uplift from exhumation histories (e.g., England and Molnar, 1990). In both cases, the distribution of relict landscapes is primarily influenced by drainage reorganization, leading to localized erosion in captured basins and the preservation of internally drained or inefficiently connected areas (Yang et al., 2015a; Jaiswara et al., 2019). Understanding these processes offers insight into long-term landscape evolution, the timing and role of tectonic activity, and how landscapes respond to large-scale climatic fluctuations, all of which are vital for comprehending the evolution of mountainous terrains over geological timescales.

Central Asia, and particularly regions such as the Tian Shan, Gobi Altai, and western Mongolia, hosts an extensive array of such low-relief surfaces that have attracted considerable scientific interest due to their potential to reveal complex histories of tectonic and climatic interactions (Fig. 1; Jolivet et al., 2007, 2010; Gillespie et al., 2017a; Morin et al., 2019). These central Asian relict surfaces are thought to reflect periods of tectonic stability following major Mesozoic to early Cenozoic tectonic events, with phases of tectonic activity including the Triassic–Early Jurassic, Late Jurassic–Early Cretaceous, and Late Cretaceous intervals (Jolivet et al., 2010, 2018; Gillespie et al., 2017a; Morin et al., 2019; He et al., 2021b). The tectonic history of the region is profoundly influenced by Mesozoic accretion–collision events along the southern Eurasian margin, commonly referred to as the Cimmerian collisions, and by the Cenozoic India–Asia collision (Yin and Harrison, 2000; Kapp et al., 2007; Jolivet et al., 2010; Glorie and De Grave, 2016). These collisional events shaped the Tian Shan region through cycles of uplift and erosion, leaving a lasting imprint on the landscape that includes the preservation of relict surfaces. Additionally, studies have suggested that the Mesozoic orogenic and subsequent collapse phases of the Mongol–Okhotsk tectonic belt may correlate with exhumation episodes observed in the Tian Shan (Gillespie et al., 2017a; Wang et al., 2018). The preservation of relict surfaces since the Mesozoic provides critical constraints on the long-term tectonic, climatic, and surface processes that have shaped the Tian Shan region (Jolivet et al., 2010, 2018; Glorie et al., 2011; Gillespie et al., 2017a; Jolivet, 2017; He et al., 2021b).

In the easternmost part of the Tian Shan, the Harlik Mountains (Harlik Shan or Karlik Tagh) stand out as a unique region where extensive high-elevation relict surfaces have been preserved along its southern flank. Thermochronological data suggest that these surfaces may have formed during the Late Cretaceous to early Paleogene, following a phase of rapid exhumation linked to tectonic activity (Gillespie et al., 2017a; Chen et al., 2020b). Subsequent limited erosion allowed the long-term preservation and stabilization of these low-relief landscapes. Although it is generally agreed that

late Cenozoic reactivation of bounding faults triggered the uplift of the Harlik Mountains, this phase of activity remains poorly constrained in terms of thermochronological data due to the minimal denudation associated with Cenozoic uplift (Cunningham et al., 2003; Gillespie et al., 2017a).

Although previous studies have explored the tectonic and climatic history of the eastern Tian Shan, key questions remain regarding the formation, preservation, and modification of relict surfaces in the Harlik Mountains. Specifically, when and how did these surfaces develop, what were the dominant tectonic and climatic controls on their evolution, and how have they been influenced by subsequent fault activity? To address these questions, this study integrates geomorphology, structural geology, and low-temperature thermochronology to reconstruct the long-term landscape evolution of the Harlik Mountains. We apply digital terrain analysis to delineate relict surfaces, assess their spatial distribution, and evaluate their relationship with regional faulting. Fluvial geomorphic analysis is conducted to examine channel steepness, knickpoint distribution, and drainage basin morphology, providing insights into river incision history and landscape adjustment to tectonic forcing. Apatite fission-track (AFT) thermochronology is used to establish the thermal history of key relict surfaces and fault zones, constraining the timing of surface formation, exhumation, and fault reactivation. By combining these approaches, we aim to clarify the interplay between tectonic and climatic processes in shaping the Harlik Mountains and provide new insights into the broader landscape evolution of the eastern Tian Shan.

2 Background

2.1 Geologic setting

The Tian Shan range, located along the southern margin of the Central Asian Orogenic Belt (CAOB; Fig. 1), comprises three main tectonic units: the northern, central, and southern Tian Shan (Windley et al., 2007; Charvet et al., 2011; Xiao et al., 2013). The Tian Shan has a complex geological history, initially marked by the accretionary collision of several microcontinents in the Paleozoic, followed by significant reworking due to strike-slip fault movement in the late Paleozoic (Windley et al., 1990, 2007; Xiao et al., 2013; He et al., 2021a). Subsequently, this region underwent several phases of intra-continental tectonic reactivation throughout the Mesozoic and Cenozoic (Windley et al., 1990; Dumitru et al., 2001). Notably, the southern Tian Shan was subjected to significant compression and thrusting due to far-field stresses from the collision between the Indian and Eurasian plates, resulting in multiple large-scale tectonic deformation episodes (Bullen et al., 2001; Sobel et al., 2006a; Macaulay et al., 2014; Bande et al., 2015; Kassner et al., 2016).

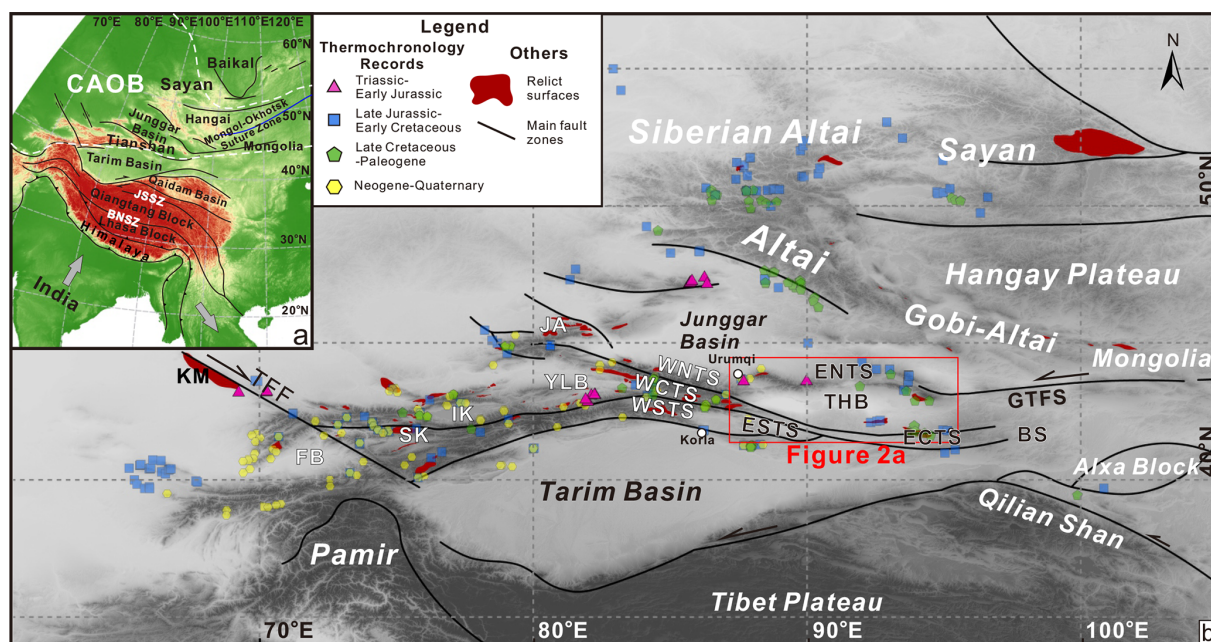


Figure 1. (a) Tectonic sketch of the Central Asian Orogenic Belt (CAOB) and adjacent regions. (b) Simplified topographic map of the Tian Shan orogenic belt and adjacent areas, showing main tectonic units and faults. Rapid cooling episodes identified through thermochronology are marked, with data sourced from De Grave and Van den Haute (2002), Zhu et al. (2004, 2007), Shen et al. (2006), Sobel et al. (2006a, b), De Grave et al. (2007, 2008, 2014), Wang et al. (2009), Zhang et al. (2009, 2011, 2016, 2021), Glorie et al. (2010, 2011, 2012a, b, 2019, 2023), Jolivet et al. (2010), Lu et al. (2013), Macaulay et al. (2014), Gao et al. (2014), Bande et al. (2015, 2017), De Pelsmaeker et al. (2015), Jia et al. (2015), Sun et al. (2015, 2021), Tang et al. (2015), Kassner et al. (2016), Tian et al. (2016), Gillespie et al. (2017a, b, 2021), Chen et al. (2018, 2020a, b), Jepson et al. (2018a, b, c, 2021b), Nachtergaele et al. (2018), Song et al. (2018), Wang et al. (2018, 2023a), Yin et al. (2018), He et al. (2021b, 2022a, 2022b, 2023; 2024), Zhimulev et al. (2021), Wu et al. (2023), and Jiang et al. (2024).

BNSZ: Bangong–Nujiang Suture Zone; BS: Beishan; ECTS: eastern central Tian Shan; ENTS: eastern north Tian Shan; ESTS: eastern south Tian Shan; FB: Fergana Basin; GTFS: Gobi–Tian Shan Fault system; IK: Issyk-Kul; JA: Junggar Alatau; JSSZ: Jinsha Suture Zone; KM: Karatau Mountains; SK: Song-Kul; TFF: Talas–Fergana fault; THB: Turpan-Hami Basin; WCTS: western central Tian Shan; WNTS: western north Tian Shan; WSTS: western south Tian Shan; YLB: Yili Block.

The Tian Shan orogenic belt is geographically divided into western and eastern segments along the Ürümqi–Korla line (Fig. 1b). These two regions exhibit distinct differences in geomorphic expression (Fig. 1b) and in their Mesozoic–Cenozoic tectonic evolution (Jolivet et al., 2010; Gillespie et al., 2017a; Chen et al., 2018; Sun et al., 2021), as discussed in Sect. 2.2. The western Tian Shan is composed of the western Chinese Tian Shan and its extension into the Tian Shan ranges of Kazakhstan, Kyrgyzstan, and Uzbekistan (Fig. 1). The eastern Tian Shan, which encircles the Turpan-Hami Basin, includes the Moqinwula, Bogda–Barkol–Harlik, and Jueluotage ranges from north to south (Figs. 1 and 2). The easternmost Tian Shan forms part of the Harlik arc, a region that developed in response to subduction of the Paleo-Asian Ocean and consists primarily of Ordovician–Carboniferous volcanic and volcanoclastic rocks (Xiao et al., 2004; Deng et al., 2016; Ji et al., 2019; Ni et al., 2021). In addition, Carboniferous and Permian igneous rocks are widespread in the easternmost Tian Shan (Ma et al., 2015). The Harlik Mountains are also dominated by Paleozoic strata, with the southern flank hosting sizable granitoid and diorite plutons, pre-

dominantly of Silurian and Carboniferous age (Fig. 2c; Ma et al., 2015; Gillespie et al., 2017a).

The Harlik Mountains lie at the boundary between the northern Tian Shan and the East Junggar arc or terrane, a location that has experienced a multi-phase tectonic evolution during the Mesozoic and Cenozoic (Chen et al., 2020a). The Harlik Mountains are structurally linked to the Gobi–Tian Shan Fault (GTF) system, a significant left-lateral strike-slip fault system that connects the eastern Tian Shan with the Gobi Altai. This fault system forms a restraining-bend termination zone featuring a horsetail fault geometry (Fig. 1; Cunningham et al., 2003; Cunningham, 2013). The Harlik Mountains thus form an asymmetrical fault-bounded structure, delimited by the North Harlik Boundary Fault (NHBF), the South Harlik Boundary Fault (SHBF), and the Barkol Fault system (BFS) (Fig. 2c). This structure is marked by substantial uplift and denudation of the Paleozoic basement rocks to the north, while the southern flank is capped by a gently dipping relict surface (Gillespie et al., 2017a).

Since the Mesozoic, tectonic activity in the easternmost Tian Shan has been influenced by a range of tectonic set-

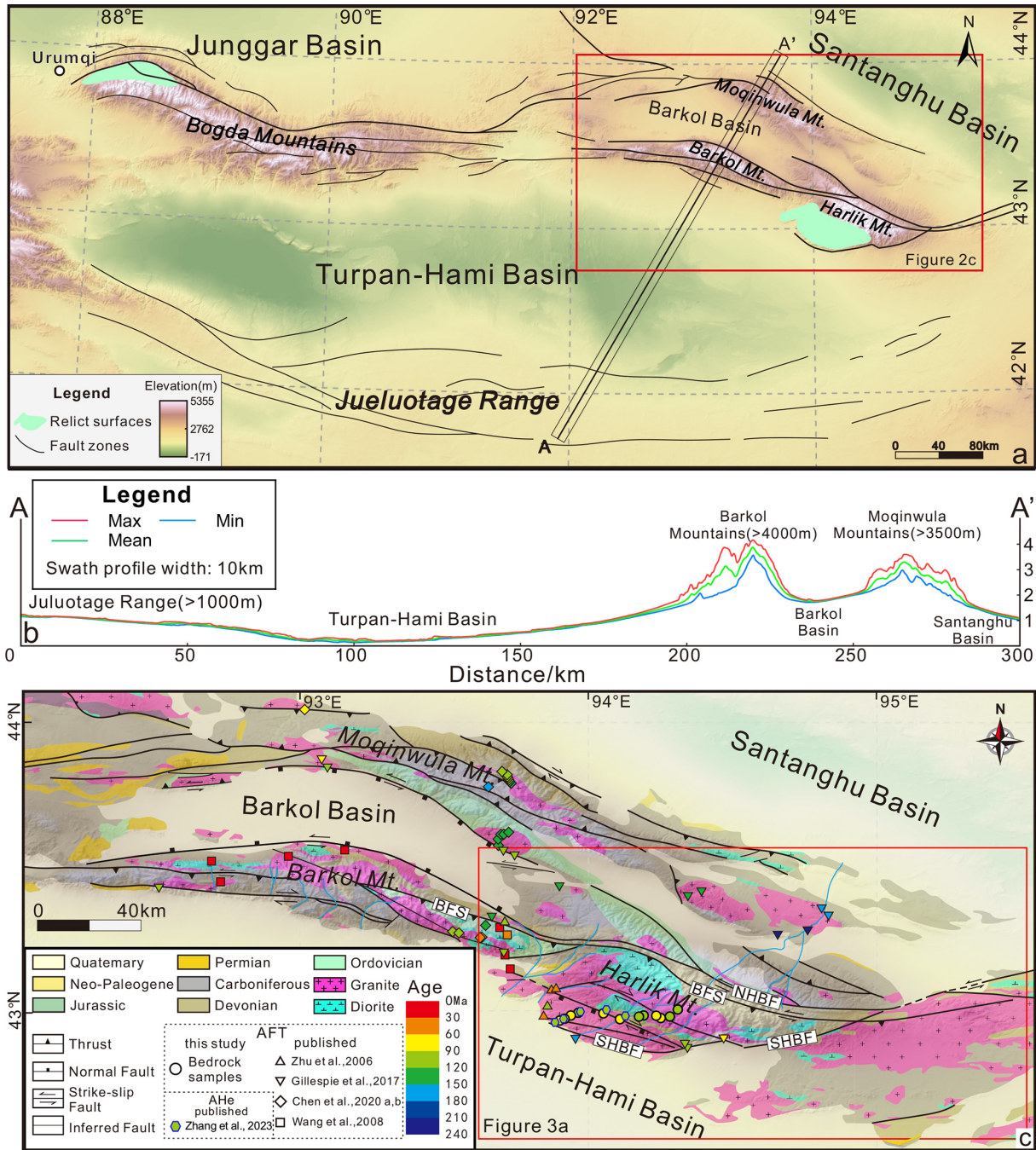


Figure 2. (a) Map showing the topography of the eastern Tian Shan and its main tectonic structures; (b) topographic cross-section A–A' from the Santanghu Basin to the Jueluotage Range; (c) simplified geological map of the easternmost Tian Shan (modified from China Geological Survey, 2007)

tings, resulting in a complex structural system. During the Late Jurassic to Early Cretaceous, deformation transitioned from compression to extension, evidenced by Late Jurassic–Early Cretaceous folding and thrust faulting in the Moqinwula Mountains (Chen et al., 2020a) and mid- to late Early Cretaceous normal faulting in the Barkol Mountains (Chen et al., 2020b). Cenozoic tectonic activity in the Harlik

Mountains is generally associated with the far-field effects of the India–Asia collision, which reactivated pre-existing fault systems and generated a characteristic southward-tilted structure (Cunningham et al., 2003; Gillespie et al., 2017a). The structural framework of the Harlik Mountains also reflects a regional transition in deformation style, from thrust-dominated deformation in the central Tian Shan to transpres-

sional deformation in the easternmost Tian Shan, driven by the interaction between the rigid Tarim craton and the more deformable Junggar block (Cunningham et al., 2003; Cunningham and Zhang, 2021).

2.2 Mesozoic–Cenozoic evolution of relict surfaces in the Tian Shan

In response to the Cenozoic India–Asia collision, individual ranges within the Tian Shan were uplifted mainly along pre-existing faults, resulting in a basin-and-range-type landscape (Sobel et al., 2006a; Jolivet et al., 2010; Chen et al., 2018; Chang et al., 2019). Despite significant uplift, extensive relicts of the low-relief Mesozoic to early Cenozoic topography are widely distributed throughout the Tian Shan region (Jolivet et al., 2010, 2018; Morin et al., 2019; He et al., 2023). These relict surfaces provide evidence of multiple phases of erosion, tectonic stability, and subsequent reactivation. However, the processes underlying the development of these relict low-relief surfaces vary across different regions of the Tian Shan.

2.2.1 Kazakh and Kyrgyz Tian Shan

In western Kazakhstan, southwest of the Talas–Fergana fault (Fig. 1), Allen et al. (2001) identified a tilted relict surface atop the Karatau Mountains. Although this surface has been dissected during the late Cenozoic, the age of its formation remains undetermined. In Kyrgyzstan, low-temperature thermochronology data indicate that high-altitude relict surfaces in the Issyk-Kul and Song-Kul areas were formed during a prolonged period of slow erosion, following a phase of significant exhumation in the Late Triassic to Early Jurassic (De Grave et al., 2011, 2013; Rolland et al., 2020). A sedimentary hiatus spanning the Middle Jurassic to Paleogene in surrounding basins, coupled with Neogene–Quaternary sediments partially covering these surfaces, suggests that they developed between the Jurassic and Paleogene (Burbank et al., 1999; De Pelsmaeker et al., 2018). However, limited apatite fission-track thermochronology data imply that the Kyrgyz Tian Shan experienced rapid exhumation during the Cretaceous (Sobel et al., 2006a; De Grave et al., 2012; De Pelsmaeker et al., 2015). Chen et al. (2018) proposed that the low-relief surfaces in Kyrgyzstan emerged during a phase of tectonic stability between the Late Cretaceous and early Cenozoic.

2.2.2 Chinese western Tian Shan

The tectonic and geomorphic evolution of the Chinese western Tian Shan during the Meso-Cenozoic parallels that of the Kyrgyz Tian Shan. In regions such as the Yili Block, western central Tian Shan, and western south Tian Shan, low-temperature thermochronology data indicate significant exhumation during the Late Triassic to Early Jurassic, followed by slower exhumation from the Middle Jurassic to Late Cre-

taceous (Jolivet et al., 2010; Wang et al., 2018; Glorie et al., 2019; He et al., 2021b, 2022b). The degree to which Late Jurassic to Early Cretaceous exhumation affected the Chinese western Tian Shan remains a topic of discussion (Dumitru et al., 2001; Jolivet et al., 2010; Wang et al., 2018; Glorie et al., 2019; Xiang et al., 2019). According to Jolivet et al. (2010), Wang et al. (2018), and He et al. (2021b), the Chinese western Tian Shan did not experience significant relief building during its Mesozoic evolution; instead, the low-relief surfaces were established during this period. A geomorphological and sedimentological investigation in the northern Chinese western Tian Shan (Jolivet et al., 2018) demonstrated that the Mesozoic relict surfaces transformed into multiphased, nested erosional surfaces, which were subsequently incised by Late Cretaceous to early Paleogene paleo-valleys.

2.2.3 Eastern Tian Shan

Recent studies have increasingly focused on the eastern Tian Shan, where relict surfaces and significant tectonic structures have been identified. Thermal history modeling of thermochronology data indicates that the primary exhumation phase in the Jueluotage Range occurred during the Triassic to Early Jurassic (Gong et al., 2021; Sun et al., 2021). This was followed by multiple exhumation pulses recorded during the Early Cretaceous and Late Cretaceous–Paleogene (Gao et al., 2014; Sun et al., 2015, 2021; Gong et al., 2021; He et al., 2022a). Different datasets independently suggest a decrease in relief in the Jueluotage range during the Jurassic. Detrital zircon geochronology from the Turpan-Hami Basin reveals a significant decline in provenance linked to the Jueluotage Range during the Middle to Late Jurassic (Shen et al., 2020; Qin et al., 2022). Both the Turpan-Hami Basin and parts of the Jueluotage Range experienced burial during Jurassic deposition (Shao et al., 1999, 2003; Gong et al., 2021; Sun et al., 2021). The low relief and elevation of the Jueluotage Range are presumably due to prolonged slow erosion during the Mesozoic and Cenozoic.

Previous thermochronological studies of the Bogda Mountains have primarily concentrated on the western portion near Ürümqi. AFT ages in the Bogda Mountains display a younging trend from southwest to northeast, reflecting progressive uplift and exhumation from the Late Jurassic to the Miocene (Tang et al., 2015). Thermal history modeling has identified two rapid exhumation events: one during the latest Jurassic to Early Cretaceous and another during the Oligocene to Miocene (Tang et al., 2015). An erosional surface (Fig. 2a) that truncates Paleozoic rocks in the Bogda Mountains is thought to have formed during a Mesozoic to Paleogene period of slow erosion between these two rapid exhumation events (Tang et al., 2015; Morin et al., 2019; He et al., 2023).

In the easternmost Tian Shan, most thermochronological data indicate exhumation primarily during the Early to Middle Triassic, Early Cretaceous, and Late Cretaceous to Paleocene (Gillespie et al., 2017a; Chen et al., 2020a, b;

He et al., 2022a). Cunningham et al. (2003) documented a tilted low-relief surface preserved in the Harlik Mountains (Fig. 2a). Gillespie et al. (2017a) reported evidence of Late Cretaceous exhumation through thermal history modeling of a sample collected from the edge of this surface, suggesting that the surface formed during the Late Cretaceous to early Paleogene and was subsequently tilted during the Cenozoic. Structural analysis and low-temperature thermochronology data indicate that the Moqinwula Mountains underwent two stages of deformation during the Late Jurassic and Late Cretaceous (Chen et al., 2020a). Chen et al. (2020a) proposed that the low-relief surfaces preserved on the summits of the Moqinwula Mountains were formed in the Early Cretaceous, between these two deformation stages.

3 Tectonic geomorphology of the Harlik Mountains

To investigate the geomorphological features of the Harlik Mountains and their relationships with the structure of the mountain range, we integrated digital elevation model (DEM)-based terrain analysis, fluvial geomorphic analysis, and structural analysis. DEM-based analysis allows the identification of relict surfaces, establishing their spatial distribution and morphological characteristics. Fluvial geomorphic analysis evaluates river incision and drainage evolution, revealing the interplay between surface evolution and fluvial erosion. Structural analysis constrains fault kinematics and paleostress regimes, clarifying tectonic controls on landscape evolution. This integrated approach enables a comprehensive reconstruction of the deformation history of the range and its geomorphic impacts.

3.1 DEM-based terrain analysis

Although relict surfaces in the Harlik Mountains have been recognized for nearly 2 decades, studies have primarily focused on their mapping and delineation using remote-sensing imagery and field surveys (Cunningham et al., 2003; Gillespie et al., 2017a). Morphologically, these surfaces are typically manifested as elevated positive-relief landforms characterized by sub-horizontal or slightly tilted planar topography (Calvet et al., 2015; Yang et al., 2015a; Liu et al., 2019).

3.1.1 Materials and methods

We employed digital terrain analysis based on the Shuttle Radar Topography Mission (SRTM) DEM, which has a resolution of 3 arcsec (~ 90 m), to extract relict surfaces in the Harlik Mountains. Low-relief areas within and around the Harlik Mountains were delineated using a topographic slope criterion of less than 14° (Calvet et al., 2015; Haider et al., 2015; Liu et al., 2019). These areas encompass potential relict surfaces and low-relief regions in valleys and basins. To isolate the relict surfaces within the mountain range, we excluded areas with a relative height of less than 40 m (Fig. 3a).

The relative height is defined as the elevation difference between the original DEM and a reference erosion surface (Haider et al., 2015). We extracted the drainage network from the DEM to identify river systems that have incised the original low-relief surfaces, using a contributing area threshold of 100 cells. A reference erosion surface was created by interpolating the elevations corresponding to the valley bottoms (i.e., the drainage lines). Figure S1 in the Supplement provides a detailed description of the extraction procedure, along with the original DEM and slope map.

3.1.2 Results

Based on the degree of preservation and the orientation of individual low-relief areas, we categorized the relict surfaces into several blocks (S1–S9 in Fig. S2 in the Supplement), as shown in Fig. 3a. To better understand the spatial relationships among the different relict surfaces, we extracted several NE–SW- and NW–SE-trending swath profiles (Fig. 3b–f). The NW–SE-trending swath profiles reveal that elevations of the relict surfaces on the southern flank of the Harlik Mountains increase towards the east. Additionally, the relict surfaces in the eastern part of the range exhibit more pronounced erosion compared to those in the west (Fig. 3b–d). The NE–SW-trending swath profiles illustrate significant topographic contrasts among these relict surfaces, with varying slopes dipping towards the south or southwest (Fig. 3e–f). Field observations indicate that these topographic contrasts are controlled by faults, which are discussed further in Sect. 3.2.

We extracted slope and aspect data for the grid points corresponding to the relict surfaces in different blocks, presented as slope-aspect rose diagrams (see Fig. S2). The primary aspects of each surface are indicated with arrows in Fig. 3a. Some surfaces are represented by fan-shaped symbols, reflecting an angular range of aspects due to the absence of distinct individual aspects. The orientations of these surfaces are significantly influenced by boundary faults, including the North Harlik Boundary Fault (NHBF), the South Harlik Boundary Fault (SHBF), and the Barkol Fault system (BFS). Surface S1, bounded by the NHBF and BFS, features a gentle slope with a predominant westward aspect. Surface S3 is also bounded by the NHBF and BFS, gently dipping towards the northeast. Surface S2, located north of the NHBF, dips northeastward, perpendicular to the orientation of the NHBF. To the south of the BFS, surfaces S4, S5, and S7 predominantly dip towards the southwest. These surfaces are constrained to the north by the BFS and appear to be cut and variably tilted by different strands of the SHBF.

3.2 Fluvial geomorphic analysis

Fluvial erosion has modified the relict low-relief surfaces on the southern flank of the Harlik Mountains, reflecting the interplay between river incision and tectonic deformation. Using the 3 arcsec resolution SRTM DEM, we analyzed

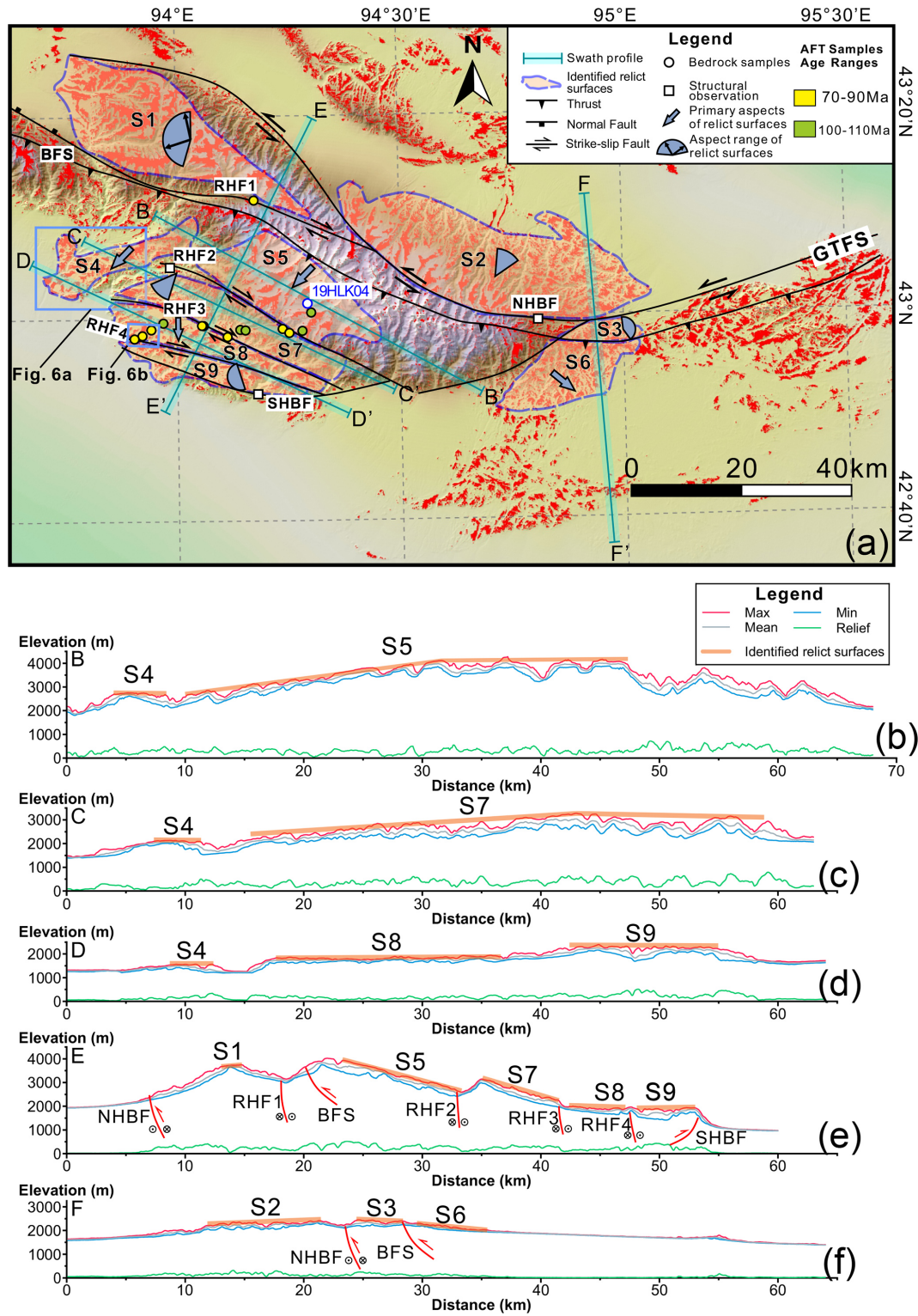


Figure 3. (a) DEM of the Harlik Mountains with low-relief areas (slope <math>< 14^\circ</math>) in red; different identified relict surfaces (indicated as S1–S9) are shown with pink shading and a dashed outline. (b–f) Topographic cross-sections B–B' to F–F' (see location in panel a). AFT: apatite fission track; BFS: Barkol Fault system; NHBF: North Harlik Boundary Fault; RHF: right-lateral strike-slip fault; SHBF: South Harlik Boundary Fault.

drainage metrics (k_{sn} and χ) to quantify incision patterns, detect transient landscape adjustments, and assess structural controls on river evolution.

3.2.1 Methods

Catchments and fluvial metrics, such as the normalized steepness index (k_{sn}) and the integral proxy (χ), were extracted using the Topographic Analysis Kit (Forte and Whipple, 2019) alongside TopoToolbox 2 algorithms (Schwanghart and Scherler, 2014). A total of basins draining the southern flank of the Harlik Mountains were extracted based on a minimum drainage area threshold of 106 m^2 . The slope (S) and contributing drainage area (A) of the river profile follow a power-law relationship (e.g., Flint, 1974; Whipple and Tucker, 1999):

$$S = k_s A^{-\theta}. \quad (1)$$

The steepness index (k_s) allows the comparison of channel gradients across different drainage areas (Flint, 1974; Whipple and Tucker, 1999; Wobus et al., 2006; Kirby and Whipple, 2012), while the concavity index (θ) quantifies the downstream decline in river gradient (Lague, 2014; Gailleton et al., 2021; Smith et al., 2022). Chi (χ) analysis is a robust method for assessing river profile evolution and detecting transient landscape adjustments. The χ parameter is defined as

$$\chi = \int_{x_b}^x \left(\frac{A_0}{A(x')} \right)^{\frac{m}{n}} dx', \quad (2)$$

where x_b represents the base-level position of the river (e.g., the river mouth), $A(x')$ denotes the upstream catchment area, m and n are empirical constants, and A_0 is an arbitrary scaling area. Under steady state, the ratio m/n corresponds to θ .

We determined an optimal concavity index, θ_{ref} , for the southern Harlik catchments using Bayesian optimization (Fig. S3 in the Supplement; Schwanghart and Scherler, 2017). The optimized θ_{ref} (~ 0.22) was then used to calculate the normalized steepness index, k_{sn} , for the river channels across all 10 basins. We selected 3 basins (1, 3, and 4) for further longitudinal profile and χ analysis, with A_0 set to 106 m^2 .

We set a 120 m tolerance for knickpoint extraction in longitudinal profiles using TopoToolbox 2 (Schwanghart and Scherler, 2014). To minimize misidentifications from DEM noise, we validated the extracted knickpoints using satellite imagery and $\chi - z$ plots. Knickpoints were then classified based on their likely origins as (1) glacial, (2) structural (potentially linked to active faults), or (3) transient, resulting from drainage reorganization or changes in tectonic uplift rates (Marrucci et al., 2018; Gong et al., 2024).

3.2.2 Results

The distribution of channel steepness (k_{sn}) aligns with the overall topographic pattern. High k_{sn} values are primarily concentrated along faults, in the eastern part of the area where no relict surfaces are preserved, and, to a lesser extent, on surface S7, whereas low values are observed on surfaces S5, S8, and S9 (Fig. 4a). Additionally, k_{sn} exhibits an increasing trend toward the east across all relict surfaces on the southern flank of the Harlik Mountains.

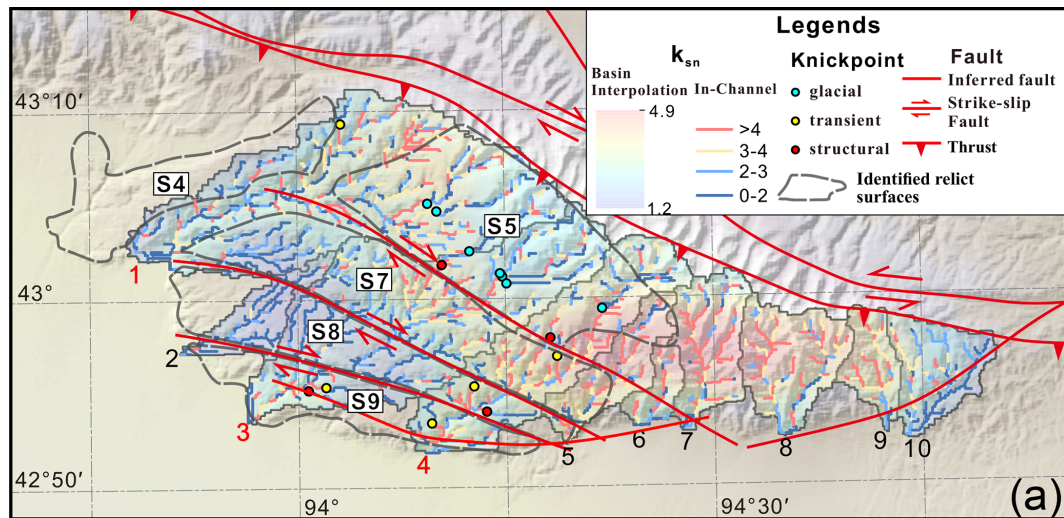
A total of 16 knickpoints were extracted from the three selected basins (Fig. 4a). Glacial knickpoints are mainly found at the base of U-shaped valleys, often occurring at tributary junctions or within hanging valleys, with elevations ranging from 3000–3500 m. In longitudinal profiles, they appear as distinct concave-up breaks (Fig. 4b–d), while, in $\chi - z$ plots, they exhibit a pronounced deviation from linearity (Fig. 4e–g). Structural knickpoints in this study are exclusively located near faults, typically within valleys incising relict surfaces. They are manifested as discrete heterogeneities along longitudinal profiles (Fig. 4c–d), indicating localized variations in channel gradient. Transient knickpoints are concentrated along tributaries extending to relict surfaces (e.g., S7–S9) and are consistently positioned near these surfaces. In longitudinal profiles, they are marked by a notable downstream increase in slope (Fig. 4b–d), accompanied by a similar trend in k_{sn} (Fig. 4a). In $\chi - z$ plots, they appear as prominent convex breaks along the curve (Fig. 4e–g).

3.3 Structural analysis

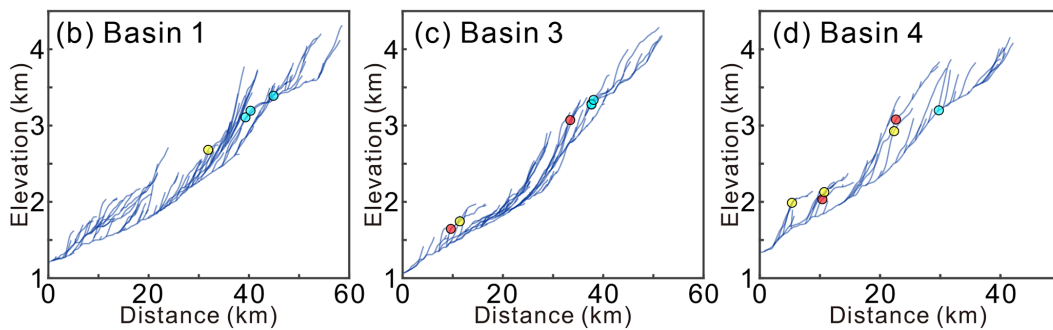
The relict surfaces in the Harlik Mountains are bounded by prominent topographic scarps visible on swath profiles, which correspond to linear boundaries in map view (Fig. 3) that correspond to faults. To better understand the formation and tectonic evolution of these surfaces, we conducted a detailed structural analysis of the Harlik fault system through field investigations.

3.3.1 Methods

In the field, we conducted a systematic investigation of the fault system in the Harlik Mountains. Fault kinematics were identified based on structural features such as slickenlines, steps, en échelon cracks, and offset markers, including veins and volcanic tuff bands. We measured the attitude of fault planes and slickenlines and performed paleostress analysis using the software Win-Tensor (Delvaux and Sperner, 2003; Fig. 5). Win-Tensor inverts fault-plane attitudes and slickenline orientations, using iterative optimization to refine principal stress axes and the stress ratio for accurate stress field reconstruction. To supplement the field observations, Google Earth imagery was utilized to identify fault-controlled landforms and accurately map fault traces (Fig. 6).



Longitudinal Profile :



χ -z plot :

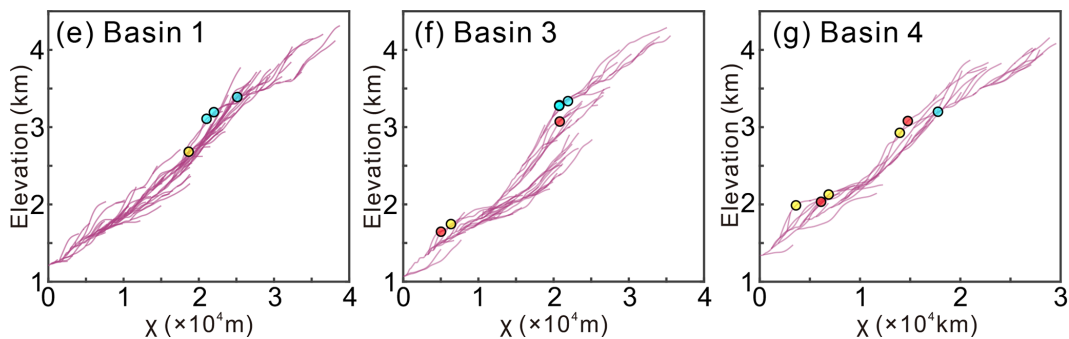


Figure 4. (a) Normalized channel steepness (k_{sn}) map of catchments draining the southern flank of the Harlik Mountains and locations of knickpoints with inferred origins overlain on shaded topographic relief. (b–d) Longitudinal profiles of the main trunk and tributaries for catchments 1, 3, and 4, with the extracted knickpoints marked. (e–g) Corresponding χ plots of these catchments, with the knickpoints indicated at their corresponding positions in χ space.

3.3.2 Results

The east–west-striking NHBF delineates the northern edge of the Harlik Mountains. This fault exhibits a southward bend before extending eastward, where it merges with the Gobi–Tian Shan Fault (Fig. 3a). Field observations reveal that the NHBF displays predominantly left-lateral oblique strike-slip movement, with the southern block moving upward relative

to the northern block. Slickenlines on the fault surface suggest a principal compressional stress direction oriented NE–SW (Fig. 5m). Similar to the NHBF, the SHBF also features low-angle thrust faults combined with high-angle left-lateral strike-slip faults (Fig. 5b and c).

Surface S1 is bordered by the NHBF to the north and by a right-lateral NW–SE-trending strike-slip fault (RHF 1) to the south (Figs. 3 and 4d). Additionally, three parallel NW–

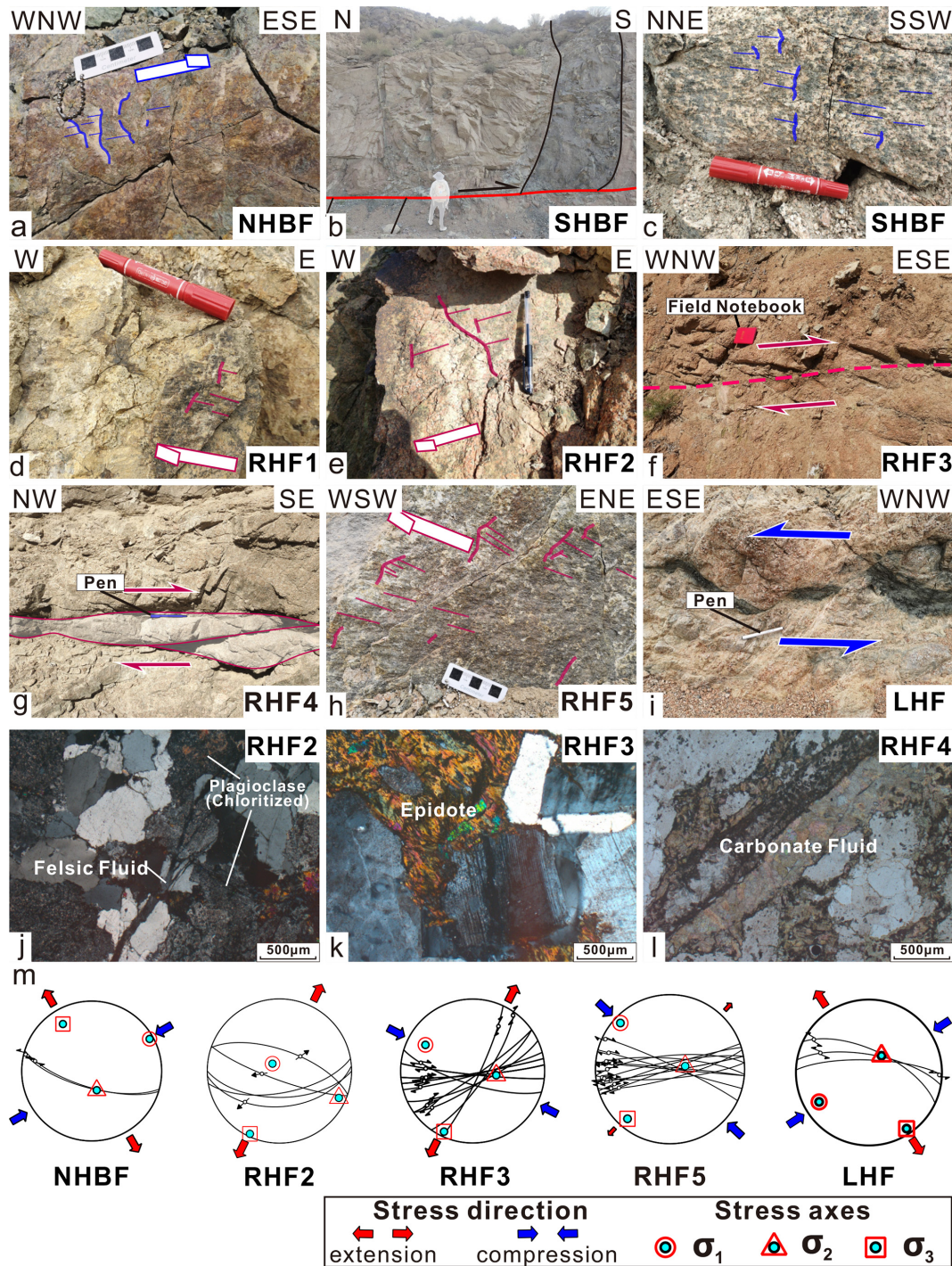


Figure 5. Outcrop photos of faults in the Harlik Mountains (a–i; locations of the study sites are shown in Fig. 3a; high-resolution versions are provided in Fig. S4 in the Supplement) and microstructural images of rocks within the fault zones (j–l). (a) Slickenlines and steps on the NHBF fault surface indicate left-lateral oblique thrust motion. (b) A low-angle thrust fault delineating the southern boundary of the Harlik Mountains, with movement indicated by offset veins. (c) Slickenlines and steps on the SHBF fault surface, reflecting left-lateral movement. (d) Slickenlines and steps on the RHF 1 fault surface, indicative of right-lateral movement. (e) Slickenlines and steps on the RHF 2 fault surface, also indicating right-lateral movement. (f) En échelon cracks on RHF 3 (viewed from above), demonstrating right-lateral motion. (g) Asymmetric granitic lenses (top view) indicative of dextral shear along RHF 4. (h) Slickenlines and steps on the RHF 5 fault surface, showing dextral movement. (i) The offset of volcanic tuff bands (top view) indicates sinistral (left-lateral) movement. (j) Chloritization of plagioclase and siliceous fluid vein observed in the RHF 2. (k) Epidote alteration in RHF 3. (l) Carbonate fluid vein in RHF 4. (m) Paleostress orientations of NHBF, RHF2, RHF3, RHF5, and LHF. Detailed fault data are provided in Table S1 in the Supplement.

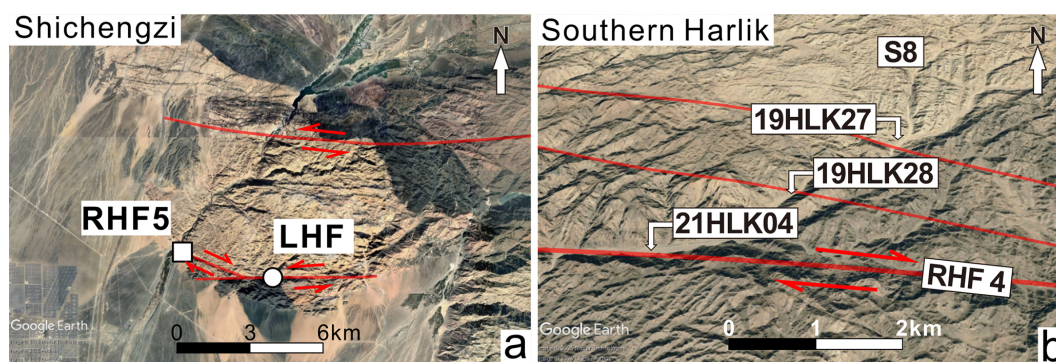


Figure 6. Google Earth imagery of the Shichengzi area (a) and RHF 4 (b); see Fig. 3a for locations. Background image: © Google Earth, Image © 2025 CNES/Airbus, Airbus, Maxar Technologies.

SE-trending faults are present along the southern flank of the range, each demonstrating right-lateral strike-slip motion (Fig. 5e–g). These faults have fragmented the relict surfaces on the southern flank into separate blocks, each dipping southwestward at various angles. Paleostress analysis of RHF 2 and RHF 3 indicates NE–SW-oriented extension, corresponding to the right-lateral movement observed along these faults (Fig. 5m). Field evidence also shows that ENE–WSW-trending left-lateral strike-slip faults subsequently overprinted these NW–SE right-lateral faults. In samples collected from these strike-slip faults, hydrothermal features are evident, including veins of siliceous and carbonate fluids associated with fault activity, along with chloritization and epidotization alterations. These characteristics differ markedly from samples taken from the low-relief surfaces, suggesting localized fluid–rock interaction during fault activity (Fig. 5j–l).

Field mapping and geomorphological analysis in the Shichengzi area of the southwestern Harlik Mountains (Fig. 3a) reveal an NW–SE-trending right-lateral strike-slip fault (RHF 5; Fig. 5h) and an ENE–WSW-trending left-lateral strike-slip fault (LHF; Fig. 5i). Remote-sensing imagery reveals that the LHF intersects RHF 5 (Fig. 6a), providing relative age constraints for these fault systems. Inferred stress tensors for these fault sets indicate NW–SE compression for RHF 5 (Fig. 5m) and NE–SW compression for LHF (Fig. 5m), further elucidating the complex, multi-phase deformation history of the Harlik fault system.

4 Low-temperature thermochronology

Low-temperature thermochronology was employed to elucidate the evolutionary history of low-relief surfaces in the Harlik Mountains. This technique serves as a valuable tool for constraining both the magnitude and timing of denudation, as fluctuations in denudation rates are often correlated with the formation, preservation, and degradation of low-relief surfaces in mountainous regions (e.g., van der Beek

et al., 2009; Rohrmann et al., 2012; Morin et al., 2019; Cao et al., 2022). Typically, tectonic activity can cause rapid exhumation, leading to relief development and fast rock cooling. As tectonic activity decreases, erosion lowers the relief, resulting in a period of slow rock cooling linked to slow denudation. A phase of thermal stability, with no significant vertical movements, corresponds to low-relief topography, until tectonic reactivation leads to renewed uplift and exhumation. In the Harlik Mountains, relict surfaces are fragmented into several blocks by faults and incised valleys, indicating a complex history of relief rejuvenation. Thus, rocks situated on these relict surfaces are expected to preserve cooling histories reflective of both relief-building and subsequent leveling processes, while those located near faults or within valleys may record late-stage cooling events linked to relief rejuvenation (e.g., Cao et al., 2022).

4.1 Sampling strategy

While previous studies have reported low-temperature thermochronology data from the Harlik Mountains, the majority of these data have been collected from the margins of the mountain belt or from the main valleys within the mountains (Zhu et al., 2006; Gillespie et al., 2017a; He et al., 2022a; Zhang et al., 2023). Consequently, the relationship between these samples and the relict surfaces or fault systems remains ambiguous. To investigate the relief evolution in the Harlik Mountains, we systematically collected samples for low-temperature thermochronology along two valleys situated on the southern flank of the mountain range. The samples encompass the four main identified blocks and the fault zones separating them. Sampling was conducted at an average elevation interval of 200–300 m, ranging from 1155–3747 m (Table 1). A detailed description of the samples, including their geographic locations and AFT age data, is provided in Table 1.

Table 1. Sample information and apatite fission track data, southern Harlik Mountains.

Location	Sample information				Ages				Track lengths			Mean D_{par} (μm)					
	No.	Location		Lith.	n	ρ_s (10^5 cm^{-2})	N_s	^{238}U (ppm)	Pooled age ($\text{Ma} \pm 1\sigma$)	$P(\chi^2)$ (%)	Dispersion (%)		Central age ($\text{Ma} \pm 1\sigma$)	MTL (μm)	SD (μm)	N	
		Lon.	Lat.	Elev. (m)													
RHF 1 fault zone	23HLK02	94.175	43.194	2783	Granite	25	6.87	553	15.63	90 \pm 5	9.1	14	91 \pm 5	12.9	1.2	100	2.5
	19HLK01	94.280	42.979	3390	Granite	15	4.33	156	8.03	109 \pm 5	100	0	110 \pm 8	12.5	2.1	35	1.1
RHF 2 fault zone	19HLK02	94.300	43.009	3747	Granite	16	6.98	454	12.93	102 \pm 3	100	0	102 \pm 6	12.4	1.5	105	1.2
	19HLK07	94.249	42.974	3097	Diorite	18	18.46	660	52.98	70 \pm 5	2.8	15	73 \pm 4	12.1	1.2	140	1.5
S7	19HLK08	94.235	42.982	2799	Diorite	18	12.21	643	29.38	84 \pm 5	33	7	86 \pm 5	12.4	1.2	82	1.5
	19HLK10	94.197	42.986	2474	Granite	20	5.71	336	13.43	84 \pm 5	90	15	86 \pm 6	12.6	1.2	61	1.2
RHF 3 fault zone	19HLK14	94.152	42.981	2152	Granite	17	5.37	369	9.97	110 \pm 3	100	0	111 \pm 7	12.8	1.3	58	1.4
	19HLK15	94.141	42.982	2026	Granite	18	6.06	335	10.96	106 \pm 4	97	17	107 \pm 7	12.5	1.6	26	1.4
S8	19HLK17	94.112	42.970	1849	Diorite	15	5.78	295	14.82	77 \pm 5	96	0	78 \pm 6	12.1	1.2	35	1.4
	19HLK22	94.058	42.989	1847	Granite	19	6.35	260	18.96	80 \pm 5	55	0	80 \pm 5	12.4	1.2	28	1.4
RHF 4	19HLK24	94.055	42.989	1869	Granite	17	8.75	236	20.69	74 \pm 4	91	0	76 \pm 6	12.9	0.9	18	1.5
	19HLK26	93.968	42.993	1619	Granite	15	3.66	201	8.92	102 \pm 3	100	0	103 \pm 8	12.0	1.4	43	1.2
RHF 4	19HLK27	93.941	42.983	1516	Granite	13	8.42	276	21.57	70 \pm 6	75	19	72 \pm 6	12.6	1.2	50	1.2
	21HLK04	93.921	42.973	1398	Granite	17	3.2	89	8.70	84 \pm 7	97	0	87 \pm 9	12.4	1.4	31	1.1
		93.903	42.968	1317	Granite	23	9.19	385	26.39	70 \pm 5	17	10	73 \pm 4	–	–	–	–

Note: Uranium content of all grains measured by LA-ICP-MS. Pooled AFT ages of all grains. Central age calculated using the RadialPlotter program (Vermeesch, 2009). Column headings are as follows: No.: sample identification number. Lon., Lat.: longitude and latitude of the sampling location. Elev. (m): elevation in meters above sea level. Lith.: lithology of the sample. n : number of analyzed grains. ρ_s (10^5 cm^{-2}): surface density of spontaneous fission tracks. N_s : number of spontaneous fission tracks counted. ^{238}U (ppm): uranium concentration in parts per million. Pooled age ($\text{Ma} \pm 1\sigma$): pooled fission track age in million years with 1 standard deviation. $P(\chi^2)$ (%): chi-square probability that the single-grain ages represent a single population age. Dispersion (%): single-grain age dispersion in percent. Central age ($\text{Ma} \pm 1\sigma$): central fission track age in million years with 1 standard deviation. MTL (μm): mean track length in micrometers. SD (μm): standard deviation of track length in micrometers. N : number of measured track lengths. Mean D_{par} (μm): mean etch pit diameter (D_{par}) in micrometers, representing annealing characteristics of apatite.

4.2 Apatite fission-track dating

4.2.1 Methods

Apatite grains were concentrated using standard heavy-liquid and magnetic separation techniques prior to being mounted in epoxy resin on glass slides. The mounted grains were subsequently ground and polished to expose their internal surfaces. These polished mounts were etched in 5 M HNO₃ for 20 s at 20 °C, following the protocols established by Gleadow et al. (2002). Apatite grains with polished surfaces parallel to prismatic crystal faces and uniform track distributions were selected for analysis. High-resolution digital images were captured in both reflected and transmitted light at a total magnification of 1000× using a Zeiss Axio Imager M1m microscope and a 3.2 MP camera. Fission-track density, confined track lengths, and etch pit diameters (D_{par}) were measured (analyst: Z. Zhao) utilizing the Trackwork and Fast track systems at the Hubei Key Laboratory of Critical Zone Evolution, School of Earth Sciences, China University of Geosciences, Wuhan. The uranium content of selected grains was analyzed using laser ablation inductively coupled plasma mass spectrometry (LA-ICP-MS). Trace-element signals were normalized against ⁴³Ca using NIST-610 as a reference standard (Pearce et al., 1997; Vermeesch, 2017). AFT ages were calibrated using the LA-ICP-MS ζ method, with Fish Canyon Tuff apatite (28.4 ± 0.1 Ma) serving as the ζ calibration standard (Hasebe et al., 2004, 2013; Vermeesch, 2017).

4.2.2 Results

AFT ages for 16 samples from the Harlik Mountains span the Early Cretaceous to the early Paleocene (111 ± 7 to 51 ± 4 Ma). Mean track lengths (MTLs) were measured for 15 of these samples, ranging from 12.0–12.9 μm (Table 1). Figure S5 in the Supplement presents the confined AFT length distributions for each sample. Most bedrock samples passed the chi-squared test (Galbraith and Laslett, 1993); radial plots for each sample are provided in Fig. S6 in the Supplement.

All but two samples (19HLK27 and 19HLK28) from the low-relief surfaces show late Early Cretaceous AFT ages (~ 110–100 Ma; Table 1; Fig. 7), consistent with previously published AFT and apatite (U–Th)/He dates from nearby locations (Zhu et al., 2006; Gillespie et al., 2017a; Zhang et al., 2023). The single-grain age dispersions in these samples are relatively low (see Fig. S6 in the Supplement), with MTLs ranging from 12.0 ($n = 43$) to 12.8 μm ($n = 58$) and D_{par} ranging from 1.0–1.4 μm (Table 1). Two samples (19HLK27 and 19HLK28) collected from relict surface S8 yielded Late Cretaceous AFT ages of 70 ± 6 Ma and 84 ± 7 Ma, respectively. Sample 19HLK27 has an MTL of 12.6 μm ($n = 50$), while sample 19HLK28 has an MTL of 12.4 μm ($n = 31$).

Samples from the right-lateral strike-slip fault zones dissecting the relict surfaces primarily exhibit Late Cretaceous AFT ages (~ 90–70 Ma; Table 1; Fig. 7). A sample col-

lected from fault RHF 1 (23HLK02) has an AFT age of 90 ± 5 Ma, with an MTL of 12.9 μm ($n = 100$). Samples adjacent to the RHF 2 fault zone (19HLK07/08/10-1) range in age from 73–84 Ma, with MTLs of 12.1 μm ($n = 140$), 12.4 μm ($n = 82$), and 12.6 μm ($n = 61$), respectively. One of these samples (19HLK07) did not pass the chi-squared test (Table 1; Fig. S6). Three samples (19HLK17/22/24) located within the RHF 3 fault zone record AFT ages ranging from 74–80 Ma, with MTLs of 12.1 μm ($n = 35$), 12.4 μm ($n = 28$), and 12.9 μm ($n = 18$), respectively. A single sample (21HK04) was collected from RHF 4, yielding an AFT age of 70 ± 5 Ma.

4.3 Thermal history modeling

4.3.1 Methods

To characterize the cooling history of rocks from various geomorphic units and tectonic locations, we employed inverse thermal history modeling using the software QTQt (version 5.8.0) to generate likely time–temperature (t–T) paths (Gallagher, 2012). QTQt utilizes a Bayesian Markov chain Monte Carlo approach, using thermochronometric data and defined t–T constraints as input. The model predicts a population of acceptable thermal histories that define a posterior probability distribution. The “expected” path represents the weighted mean thermal history derived from this posterior distribution. For modeling purposes, the samples were divided into two categories: relict-surface samples (Fig. 8) and fault-zone samples (Fig. 9). Additionally, thermal histories were modeled for the two younger samples (19HLK27 and 19HLK28) collected from the low-relief surface S8 to explore potential causes for these anomalously young ages.

The AFT data were modeled using the multi-kinetic annealing model of Ketcham et al. (2007), with D_{par} serving as the kinetic parameter. Inversion was constrained solely by the current surface temperature, which was set at 10 ± 10 °C. General prior ranges were established as AFT central age ± AFT central age for time and 70 ± 70° for temperature. The software executed 200 000 burn-in iterations followed by 200 000 post-burn-in iterations to achieve stable results. For discussion purposes, cooling rates are classified empirically into three categories: slow (< 0.5 °C Ma⁻¹), moderate (0.5–2 °C Ma⁻¹), and rapid (> 2 °C Ma⁻¹) cooling (He et al., 2022a).

4.3.2 Results

The modeling result for sample 19HLK02 from surface S5 indicates a relatively steady cooling trajectory from ~ 130 Ma, with a phase of moderate cooling occurring between 130 and 100 Ma (~ 0.9 °C Ma⁻¹; Fig. 8a). Similarly, samples from surface S7 (19HLK14 and 19HLK15) exhibit steady cooling from ~ 130 Ma, with accelerated cooling rates dur-

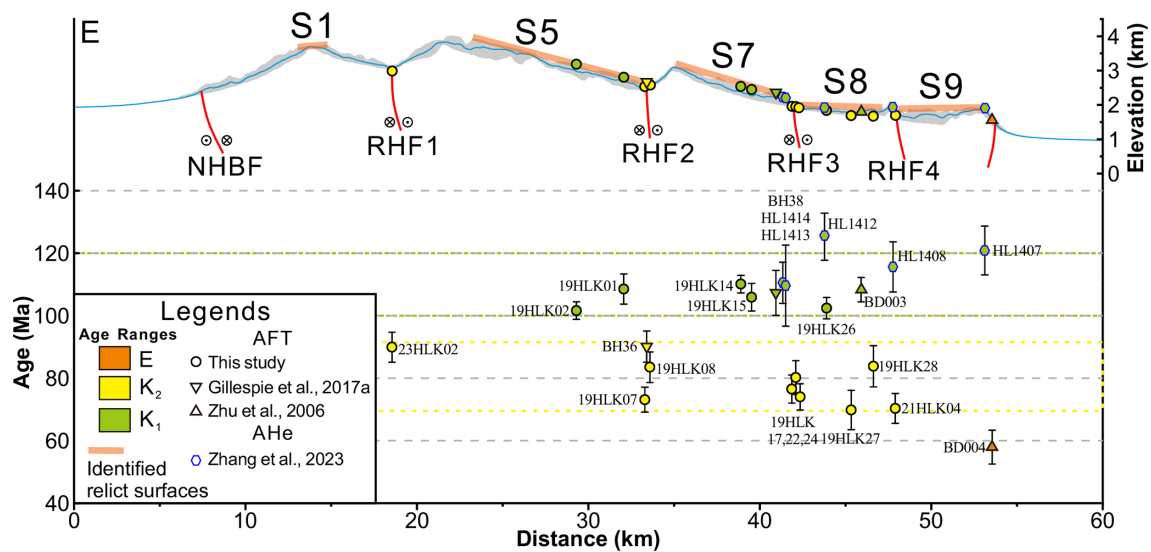


Figure 7. AFT and (U–Th)/He data projected onto profile E–E'. AFT and (U–Th)/He data from different sources are plotted with different symbols, and colors indicate ages (green: Early Cretaceous; yellow: Late Cretaceous; orange: Paleogene); see Fig. 3a for sample locations.

ing the 130–100 Ma interval ($1.1\text{ }^{\circ}\text{C Ma}^{-1}$) compared to the post-100 Ma phase ($0.5\text{ }^{\circ}\text{C Ma}^{-1}$; Fig. 8b).

In contrast, the thermal history of samples collected from surface S8 is more variable. Sample 19HLK26, situated away from the fault boundaries, displays a thermal history akin to that of the sample from surface S5, showing moderate cooling ($0.8\text{ }^{\circ}\text{C Ma}^{-1}$) in the late Early Cretaceous, followed by slow cooling ($< 0.5\text{ }^{\circ}\text{C Ma}^{-1}$; Fig. 8c). Conversely, samples 19HLK27 and 19HLK28 record cooling starting at ~ 90 Ma, with a relatively rapid cooling rate of $1.9\text{ }^{\circ}\text{C Ma}^{-1}$ until 70 Ma, which is faster than the cooling rate observed for sample 19HLK26 during the 130–100 Ma phase (Fig. 8d).

Overall, the QTQt modeling results for samples collected from the relict surfaces in the Harlik Mountains indicate a rapid cooling phase between 130 and 100 Ma, followed by a period of stable, slow cooling. Notably, some samples from surface S8 also experienced accelerated cooling 20–30 Ma later, around 90–70 Ma. Remote sensing reveals several minor faults intersecting these sample locations (Fig. 6b). All modeled thermal histories also suggest somewhat more rapid cooling from $\sim 40^{\circ}$ to surface temperatures during the last ~ 20 Ma.

Samples from the fault zones RHF 2 (19HLK07) and RHF 3 (19HLK17, 19HLK22, and 19HLK24) exhibit similar t–T paths, characterized by rapid cooling during the Late Cretaceous ($\sim 90\text{--}70$ Ma) at a rate of $\sim 1.8\text{ }^{\circ}\text{C Ma}^{-1}$ (Fig. 9b and c), followed by a transition to slower cooling. The thermal history of RHF 1 (23HLK02) is comparable to that of samples from RHF 2 and RHF 3, but it records a slightly earlier rapid cooling phase ($2.3\text{ }^{\circ}\text{C Ma}^{-1}$) around 100–90 Ma (Fig. 9a). These thermal histories also show rapid late-stage cooling from 40–50° to surface temperatures during the last 10–20 Ma.

5 Discussion

5.1 Early Cretaceous exhumation of the eastern Tian Shan

Thermal history models for samples from the low-relief surfaces record a relatively rapid rock-cooling and exhumation event during the Early Cretaceous in the eastern Tian Shan (Fig. 10). Such a thermal history contrasts to that in the Yili Block (Wang et al., 2018; He et al., 2022b), the Chinese central Tian Shan (Jolivet et al., 2010), and the Jueluotage Range (Sun et al., 2021), where exhumation is less pronounced during the Late Jurassic to Early Cretaceous. The low-relief surfaces in the central Tian Shan are argued to have formed during the Jurassic and to have been maintained under these relatively stable conditions (Jolivet et al., 2010; He et al., 2021b, 2022b). Cooling during the Late Jurassic to Early Cretaceous was more significant in the Kyrgyz Tian Shan compared to the Chinese western Tian Shan (Sobel et al., 2006a; De Grave et al., 2012; De Pelsmaeker et al., 2015). The spatial distribution of this exhumation event in the Kyrgyz Tian Shan and the Chinese western Tian Shan (Fig. 1) suggests propagation of uplift and exhumation from the southwest towards the northeast, consistent with deformation and exhumation driven by the collision of the Lhasa block with Eurasia during the Late Jurassic to Early Cretaceous ($\sim 160\text{--}120$ Ma; Kapp et al., 2007; Ma et al., 2017; Lai et al., 2019; Hu et al., 2022).

Importantly, the available thermochronology data from the low-relief surfaces in the Harlik Mountains do not indicate any cooling events predating the Cretaceous. Evidence of rapid cooling prior to the Early Cretaceous is generally limited in the easternmost Tian Shan, with a signal of Triassic cooling preserved only on the fringes of the region, outside

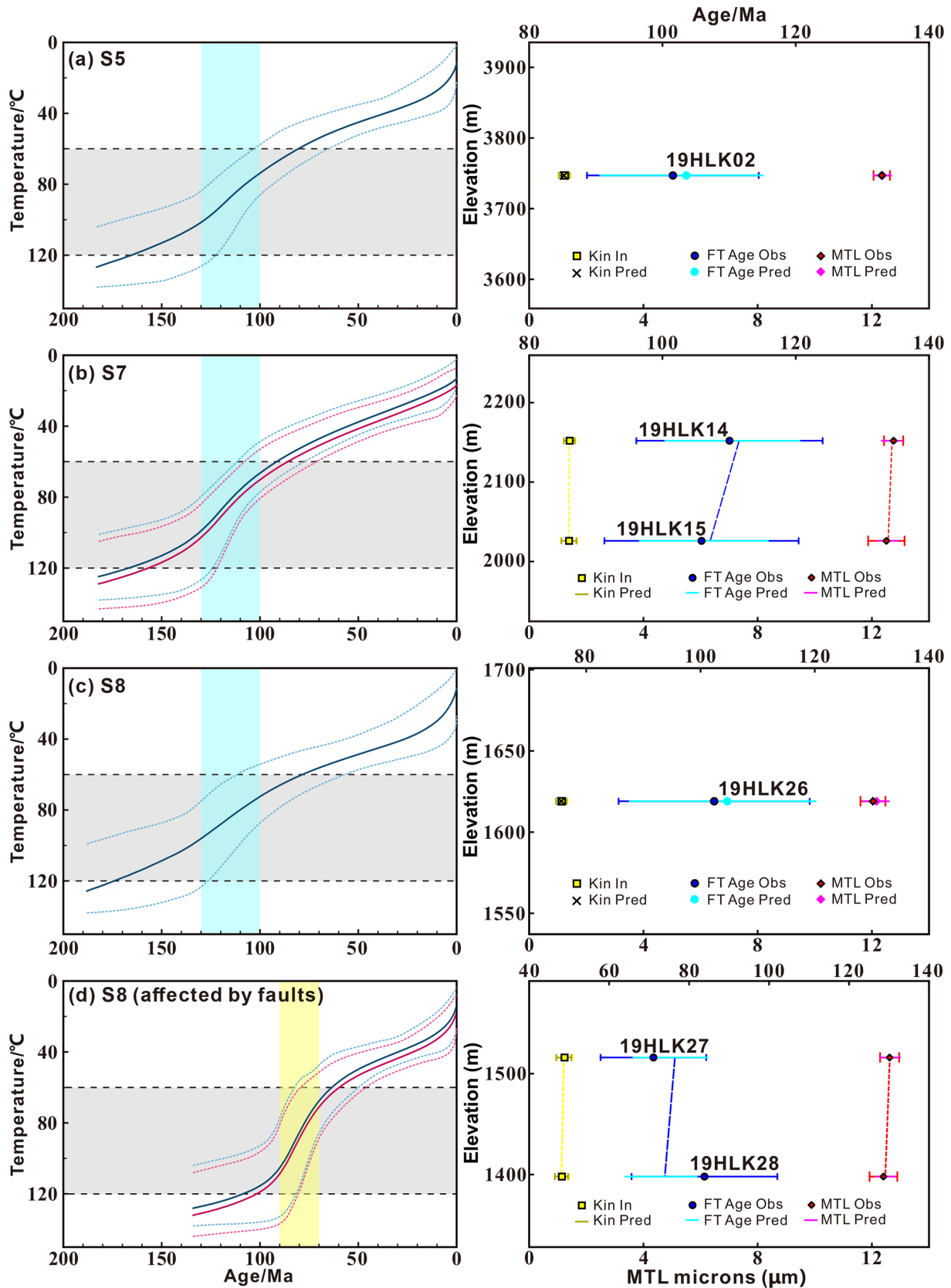


Figure 8. Thermal history models based on AFT data for samples from relict surfaces on the southern flank of the Harlik Mountains (easternmost Tian Shan) generated using the software QTQt (Gallagher, 2012). Right panels show fit to the observed AFT ages and MTL.

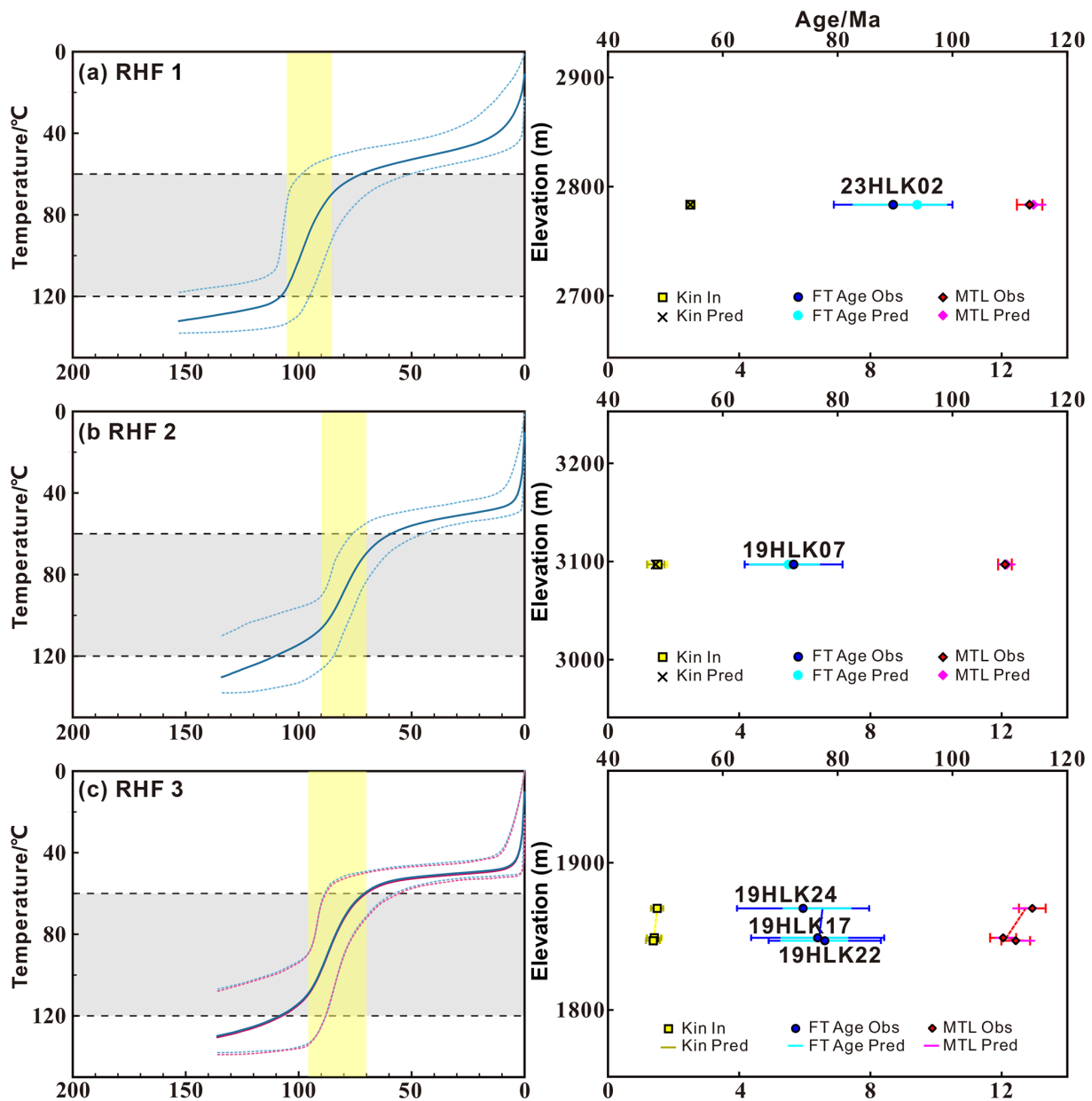


Figure 9. Thermal history models based on AFT data for samples from fault zones on the southern flank of the Harlik Mountains (easternmost Tian Shan) generated using the software QTQt (Gallagher, 2012). Right panels show fit to the observed AFT ages and MTL.

the main fault-bound ranges (Gillespie et al., 2017a; Chen et al., 2020a). This is consistent with sedimentological evidence suggesting that the easternmost Tian Shan was in an extensional setting during the Late Triassic to Middle Jurassic, characterized by slow subsidence and relatively gentle topography, with no indication of significant uplift or exhumation during this period (Chen et al., 2019). This implies that low-relief topography likely existed in the easternmost Tian Shan prior to the Early Cretaceous but was subsequently altered by tectonic deformation and associated exhumation during this period (Fig. 10c).

The compressional deformation identified in the Junggar Basin, easternmost Tian Shan, Turpan-Hami basin, and Beishan regions during the Middle to Late Jurassic (Zhu et al., 2004; Chen et al., 2020a; Guan et al., 2021; Liu et al., 2023) was likely influenced by the initial closure of the western Mongol–Okhotsk Ocean and the Lhasa–Qiangtang collision (Zhang et al., 2019; Wang et al., 2022; Liu et al., 2023). However, low-temperature thermochronology records in regions such as the easternmost Tian Shan, East Junggar, Beishan, Gobi Altai, and Altai-Sayan predominantly show cooling during the mid-Cretaceous (Jolivet et al., 2007; Glorie

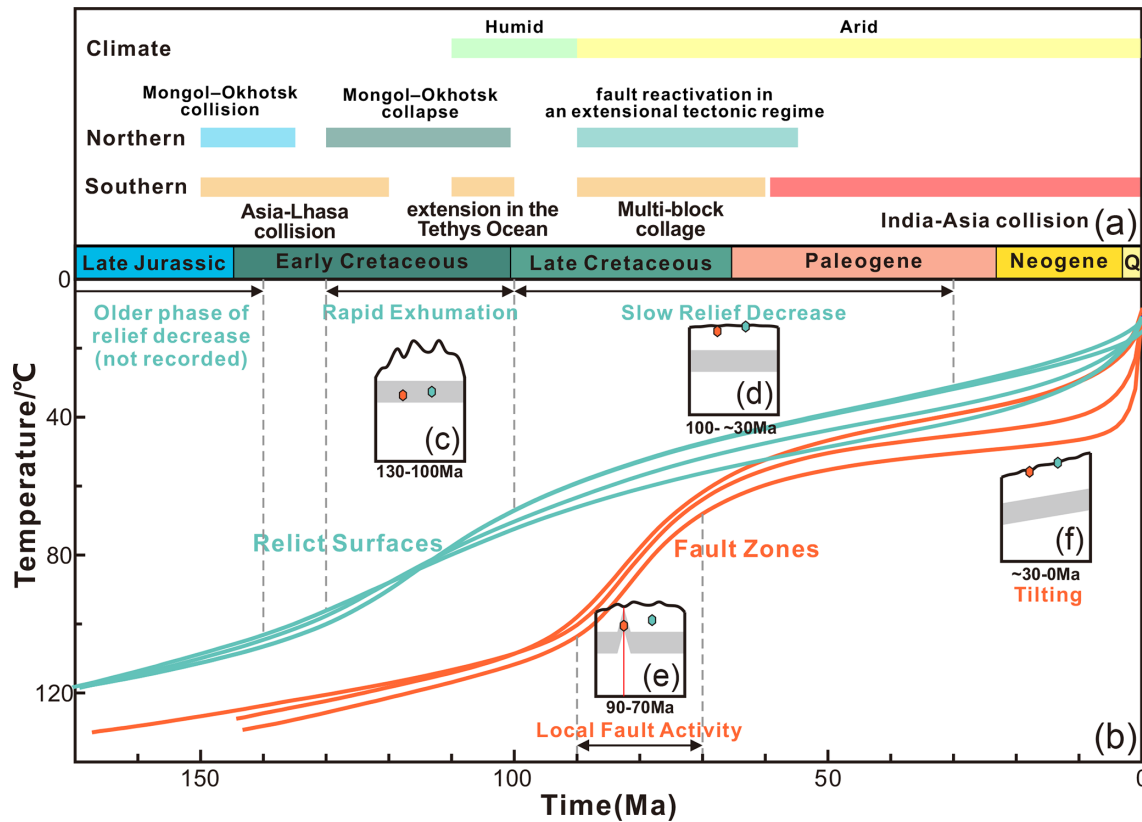


Figure 10. (a) Possible driving factors for the tectonic and geomorphological evolution of the easternmost Tian Shan. (b) Geomorphological and tectonic significance of the inferred exhumation history of the Harlik Mountains (time–temperature curves are in green for the relict surfaces and in red for the fault zones). (c–f) Sketches of the envisaged evolution of the relict surfaces, where the gray zone represents the partial annealing zone of apatite fission tracks and where relative locations of samples located on the relict surface (green dots) and in the fault zones (red dots) are shown: (c) rapid exhumation, (d) slow-relief decrease, (e) local fault activity, (f) tilting.

et al., 2012a; De Grave et al., 2014; Chen et al., 2020a, b; He et al., 2022a; Liu et al., 2023). Cooling associated with normal-fault footwall exhumation during the mid- to late Early Cretaceous is recorded in both the Barkol Mountains (128–110 Ma; Chen et al., 2020b) and the Beishan area (~124–115 Ma; Liu et al., 2023). Early Cretaceous rift-related basalts (~126–99 Ma) are also common in southern Mongolia, the Alxa Block, and the northern Qilian Shan (Graham et al., 2001; Tang et al., 2012; Hui et al., 2021). The normal faults and basalts mentioned above are considered to be associated with late Mesozoic regional crustal extension (Chen et al., 2003; Meng, 2003; Liu et al., 2023). By this time, significant deformation associated with the Lhasa–Qiangtang collision or the closure of the Mongol–Okhotsk Ocean had ceased (Fig. 10a; Wang et al., 2015; Yang et al., 2015b; Li et al., 2017; Ma et al., 2017), making it unlikely that exhumation during this period in the easternmost Tian Shan can be directly attributed to far-field effects related to these orogenies. Instead, subsequent tectonic events, such as the collapse of the Mongol–Okhotsk orogen (Fig. 10a; ~145–100 Ma; Donskaya et al., 2008; Wang et al., 2015; Yang et al., 2015b) and the break-off of the

Bangong–Nujiang Ocean slab (Fig. 10a; latest Early Cretaceous; Sui et al., 2013; Wu et al., 2015; Liu et al., 2018), likely played more significant roles in shaping the landscape of the study area. As the break-off of the Bangong–Nujiang Ocean slab was later, short-lived (Fig. 10a), and distant from the eastern Tian Shan (Fig. 1a), the collapse of the Mongol–Okhotsk orogen is more likely to have provided an extensional setting for the easternmost Tian Shan and adjacent areas during the mid- to late Early Cretaceous. The relative positions of these tectonic units are illustrated in Fig. 1a.

On the other hand, climate change may have accelerated erosion in the eastern Tian Shan and Altai regions during the mid-Cretaceous (Hendrix et al., 1992; Pullen et al., 2020; Jepson et al., 2021a). Sedimentary records from the Junggar Basin indicate a transition from arid to semi-arid conditions during the Jurassic–Early Cretaceous, evolving into seasonally wet conditions by the mid-Cretaceous (Hendrix et al., 1992; Allen and Vincent, 1997; Eberth et al., 2001). Prior to ~135 Ma, the depositional environment of the Turpan–Hami Basin transitioned from an erg environment characterized by extensive eolian cross-bedded sandstones of the Liushuquan Formation to a fluvio-lacustrine setting represented by the

Dahaidao Formation (Wang et al., 2017; Zheng et al., 2023; Zhang et al., 2024). Although positive topography may have developed in the easternmost Tian Shan by the Middle to Late Jurassic, the arid climate may have limited significant erosion. Conversely, the more humid climate of the mid-Cretaceous likely could have intensified erosion, contributing to fluvio-lacustrine sedimentation in the surrounding basins.

5.2 Local fault activity during the Late Cretaceous to early Paleogene

Our geomorphological and structural analysis reveals that several right-lateral strike-slip faults segment the relict surfaces on the southern flank of the Harlik Mountains (Fig. 3). AFT ages from samples collected within these fault zones are mainly Late Cretaceous (~ 90–70 Ma), notably younger than the cooling ages of > 100 Ma recorded on the surrounding low-relief surfaces. Rock cooling generally results from either erosional or tectonic (normal-faulting-controlled) exhumation or from thermal disturbance. Our observations show no significant differential erosion between these fault zones and the surrounding regions. Given that the faults are classified as right-lateral strike-slip rather than normal faults, the most plausible explanation for the differing cooling ages is thermal disturbance within the fault zones. Microstructural analysis of the rocks within these zones provides evidence for the presence of siliceous and carbonate fluids, indicating that these rocks were influenced by hydrothermal activity associated with faulting (Fig. 5j–l). This hydrothermal activity may have reset the AFT system in these rocks (Fig. 10e). Consequently, the observed cooling ages establish a minimum timing for fault activity, suggesting that faulting occurred during the 90–70 Ma interval. Concurrently, the cooling rate of the rocks on the relict low-relief surfaces began to slow down, indicating that regional uplift and erosion were gradually diminishing (Fig. 10d). During this time, deformation in the eastern Tian Shan was primarily governed by these right-lateral strike-slip faults.

Throughout the Late Cretaceous, both the southern and northern tectonic belts of the Tian Shan exhibited relatively low levels of tectonic activity. Consequently, many of the relict low-relief surfaces in the Tian Shan region are believed to have formed during this period (Sobel et al., 2006b; Chen et al., 2018, 2020b). While cooling events during the Late Cretaceous are less frequently recorded than those from the Early Cretaceous, they are still widely reported across central Asia (Sobel et al., 2006a; Jolivet et al., 2010; Glorie et al., 2012a, b; De Grave et al., 2013, 2014; De Pelsmaeker et al., 2015; Chen et al., 2020a). In the Tethys tectonic domain, the collision and amalgamation of island arcs, such as Kohistan, Dras, and Ladakh (Fig. 10a; Yuan et al., 2021; Andjic et al., 2022), are thought to have generated a compressive stress field, reactivating inherited Paleozoic structures within the western Tian Shan (Schwab et al., 2004; Jolivet et al., 2010; Chen et al., 2018). Field evidence, in-

cluding fault gouge zones, overprinted mylonitic fabrics, and reactivated thrust faults identified in the Narat and Bayanbulak regions, suggests multiple episodes of reactivation affecting pre-existing Paleozoic faults (Jolivet et al., 2010; Chen et al., 2018). Thermochronological constraints from AFT and apatite (U–Th)/He dating reveal significant exhumation and renewed faulting during the Late Cretaceous to early Paleocene (65–60 Ma), with deformation persisting into the Cenozoic (Jolivet et al., 2010; Chen et al., 2018). During the Late Cretaceous and early Paleogene, with the exception of these localized fault zones, the broader western Tian Shan experienced slow cooling and tectonic quiescence, facilitating the development of widespread planation surfaces (e.g., Bazhenov, 1993; Burbank et al., 1999; Glorie et al., 2010).

While the collapse of the Mongol–Okhotsk orogen has been proposed as a potential driver of extension during the mid- to late Early Cretaceous, some studies suggest that its influence persisted into the Late Cretaceous (van der Beek et al., 1996; Jolivet et al., 2009; Glorie et al., 2012a; De Grave et al., 2014), possibly contributing to fault activation in the Harlik Mountains at 90–70 Ma. Evidence for Late Cretaceous rock cooling within a northeast–southwest extensional context has been reported in the eastern Tian Shan (Song et al., 2023), Altai (Glorie et al., 2012b), Siberian Altai (Glorie et al., 2012a), Sayan (De Grave et al., 2014), and Beishan (Liu et al., 2023; Wang et al., 2024), bearing witness to widespread Late Cretaceous fault reactivation (Fig. 1b). The recorded fault activity in the Harlik Mountains during 90–70 Ma likely represents similar fault reactivation. A comparison of the tectonic setting in the northern (Glorie et al., 2012a; De Grave et al., 2014) and southern (Yuan et al., 2021; Andjic et al., 2022) tectonic belts of the Tian Shan suggests that Late Cretaceous fault (re)activation in the easternmost Tian Shan was likely associated with extensional tectonics resulting from the collapse of the Mongol–Okhotsk orogen. The lithospheric adjustments following the collapse of the Mongol–Okhotsk orogen triggered a large-scale reorganization of regional stress across NE Asia (Zhang et al., 2019), facilitating widespread crustal extension that may have extended to regions far beyond the suture zone, including the eastern Tian Shan (Song et al., 2023). Additionally, mantle upwelling related to the post-collisional extensional regime could have further contributed to the observed tectonic reactivation (Zhang, 2014).

The Tian Shan–Altai–Sayan region also experienced wetter climatic conditions during the mid-Cretaceous, followed by a drier climate from the Late Cretaceous to the present (Jepson et al., 2021a). This shift to relatively arid conditions in the study area would have restricted the extent of exhumation during this period, facilitating the preservation of low-relief relict landscapes and allowing older thermochronological cooling ages to be retained.

5.3 Cenozoic reactivation and fluvial incision of the eastern Tian Shan

During the period from 90–70 Ma, the active right-lateral strike-slip faults in the eastern Tian Shan did not induce significant differential exhumation, and rapid exhumation ceased across most areas during that time. Thermal modeling indicates a marked slowdown in cooling rate for low-relief surface samples after 100 Ma, likely coinciding with the onset of planation.

During the Cenozoic, activity in the Mongol–Okhotsk tectonic belt largely waned. To the south of the Tian Shan, the collision between the southwestern margin of the Eurasian and Indian continents led to multi-stage uplift and expansion of the Qinghai–Tibetan Plateau (Fig. 10a; Wang et al., 2011; van Hinsbergen et al., 2012; Ding et al., 2022; Suo et al., 2022). The Cenozoic India–Eurasia collision caused significant deformation in the Tian Shan and surrounding regions, reactivating pre-existing structures formed during the Paleozoic amalgamation and subsequent intra-continental deformation (Molnar and Tapponnier, 1975; Burchfiel et al., 1999). Low-temperature thermochronology analyses indicate that recent and ongoing deformation and reactivation in the Tian Shan began in the Oligocene–Miocene (De Grave et al., 2007; Chen et al., 2022; Wang et al., 2023b; Jiang et al., 2024), marking the formation of the modern Tian Shan topography. In the eastern Tian Shan, the left-lateral strike-slip Gobi–Tian Shan Fault (GTF) was reported to be active during the Cenozoic (Cunningham et al., 2003), although direct age constraints for its Cenozoic activity are lacking. This fault developed into a positive flower system in the Harlik Mountains, which functions as a restraining bend for the left-lateral strike-slip fault (Cunningham et al., 2003; Cunningham, 2007). This fault system facilitated exhumation of the Harlik Mountains and tilting of previously formed relict surfaces (Cunningham et al., 2003; Cunningham, 2007; Gillespie et al., 2017a). The accelerated cooling identified after ~ 30 Ma in our thermal models likely corresponds to this late-stage exhumation phase. Moreover, following a period of non-deposition from the Late Cretaceous to the Eocene (Shen et al., 2020), the Turpan–Hami and Barkol basins began receiving sediments again during the Oligocene to Miocene (Chen et al., 2019; Ding et al., 2024). This renewed sedimentation indicates that the Harlik Mountains have been more actively eroding since that time, marking the conclusion of relict surface development and initiating a new phase of landscape evolution in the region (Fig. 10f).

Recent apatite (U–Th)/He (AHe) data from the erosion surfaces of the southern Harlik Mountains (Zhang et al., 2023) show similar late Early Cretaceous ages to our AFT data, supporting rapid cooling during this time interval. Moreover, these data limit the amount of Cenozoic exhumation in the Harlik Mountains to less than 2 km, assuming a thermal gradient of $25\text{ }^{\circ}\text{C km}^{-1}$, a surface temperature of

$20\text{ }^{\circ}\text{C}$, and a closure temperature of $\sim 70\text{ }^{\circ}\text{C}$ for AHe. Shen et al. (2024) recently documented that the Gobi–Tian Shan Fault (GTF) is active in the Quaternary, with left-lateral slip rates of $1.1\text{--}1.4\text{ mm yr}^{-1}$ and approximately 0.7 mm yr^{-1} of north–south crustal shortening across the Harlik Mountains. Although no direct thermochronological evidence currently confirms Cenozoic tectonic activity, knickpoint analysis identifies a series of structural knickpoints along right-lateral strike-slip faults on the southern slope of the Harlik Mountains, suggesting that these faults were active during the Cenozoic (Fig. 4). A limited number of Oligocene AHe ages have been reported from the Barkol Mountains, potentially linked to tectonic activity, including fault reactivation (Zhang et al., 2023). Therefore, the vertical displacement on major faults in the easternmost Tian Shan may be associated with only limited erosion, similarly to the western Chinese Tian Shan, where recent crustal thickening and uplift has been shown to outpace erosion (Charreau et al., 2017, 2023).

The Cenozoic climate of the easternmost Tian Shan, characterized by aridity as revealed by paleoclimate simulations (Jepson et al., 2021a), limited erosion and confined it primarily to river valleys and the mountain front. The θ_{ref} value for basins on the southern flank of the Harlik Mountains is ~ 0.22 , significantly lower than the ~ 0.4 in the Kyrgyz Tian Shan (Gong et al., 2024). This difference may result from the dominance of high-strength granite in which these valleys are incised (Fig. 2c) and the arid climate, both of which can reduce θ values (Kirby and Whipple, 2001; Zaprowski et al., 2005). Additionally, transient knickpoints on the southern slope of the Harlik Mountains are concentrated near relict low-relief surfaces. In longitudinal profiles, they separate an upstream unadjusted segment from a steepened downstream reach with higher incision rates. These knickpoints thus appear to record slow headward propagation and incision of the drainage into the relict surfaces, which would have started ~ 30 Ma. Due to limited surface erosion, crustal exhumation was insufficient to induce cooling of the basement and produce younger thermochronological ages. These conditions allowed the preservation of large-scale Mesozoic low-relief surfaces in the Harlik Mountains, even though they were deformed and tilted during late Cenozoic compression. Following uplift, there is no clear evidence of drainage reorganization that would have led to the formation of in situ low-relief surfaces.

6 Conclusions

This study integrates thermochronological, structural, and geomorphological analyses to reconstruct the Mesozoic–Cenozoic landscape evolution of the Harlik Mountains in the easternmost Tian Shan. Our findings reveal a complex interplay between tectonic reactivation, faulting, and climate influences shaping the long-term geomorphic evolution of the region. The key conclusions are as follows:

1. During the Early Cretaceous (130–100 Ma), rapid exhumation and rock cooling in the Harlik Mountains were primarily driven by tectonic processes associated with the collapse of the Mongol–Okhotsk orogen. Mid-Cretaceous climatic shifts, marked by increased humidity, likely enhanced erosion, contributing to basin sedimentation and modifying the regional landscape.
2. In the Late Cretaceous (90–70 Ma), right-lateral strike-slip faulting, occurring under an extensional regime, segmented the relict surfaces but did not induce significant topographic changes. Cooling patterns and fault reactivation were likely influenced by the ongoing collapse of the Mongol–Okhotsk orogen, with aridification progressively reducing erosion rates. The initiation of widespread low-relief surfaces during this period coincided with a deceleration in exhumation and cooling rates.
3. Renewed tectonic activity during the Cenozoic (~30 Ma to present), driven by far-field effects of the India–Eurasia collision, resulted in uplift and tilting of the Harlik Mountains, shaping the modern topography of this region. Despite active faulting and basin sedimentation, relatively low erosion rates facilitated the long-term preservation of Mesozoic low-relief surfaces. The fluvial geomorphic analysis suggests that these preserved landscapes were uplifted by late-stage faulting but not significantly altered by drainage reorganization.

While this study provides new insights, several limitations should be acknowledged:

1. *Incision rates and erosion dynamics.* The lack of cosmogenic nuclide dating (e.g., ^{10}Be exposure ages) prevents a precise assessment of incision rates and erosion magnitudes. Future studies incorporating these methods could better constrain surface processes.
2. *Climate–tectonic interactions.* While this study emphasizes the role of climate in erosion, a more detailed quantitative assessment, potentially through sediment provenance analysis or numerical modeling, would improve the understanding of climate-driven landscape evolution.
3. *Active deformation constraints.* This study primarily reconstructs Mesozoic to early Cenozoic fault reactivation based on geological and geomorphic evidence. Integrating geodetic and seismic data in future research could provide further constraints on ongoing deformation.

The Mesozoic–Cenozoic landscape evolution of the eastern Tian Shan resulted from the interaction of regional tectonic (stress-field) evolution, local faulting, and climatic influences, which together shaped exhumation, deformation,

and erosion patterns. The preservation of low-relief surfaces reflects the combined effects of these processes over geological timescales. This study highlights the importance of integrating geomorphic, structural, and thermochronological data to improve understanding of landscape evolution in active orogenic systems. Future research will further refine the understanding of the complex relationships between tectonics, climate, and surface processes in the region.

Code availability. The QTQt software used for thermal history modeling and inverse modeling of thermochronological data was developed by Kerry Gallagher and is publicly available at <https://www.earth.edu.au/codes/QTQt/>, last access: 15 October 2022 (Gallagher, 2012). The RadialPlotter program, used for calculating central ages of apatite fission-track data and generating radial plots, was developed by Pieter Vermeesch and is available for download at <https://www.ucl.ac.uk/~ucfbpve/radialplotter/>, last access: 8 March 2024 (Vermeesch, 2009). The TopoToolbox 2 and Topographic Analysis Kit (TAK) software, used for fluvial geomorphic analysis in this study, are publicly available at <https://github.com/wschwaghart/topotoolbox.git>, last access: 27 January 2024 (Schwanghart and Scherler, 2014), and <https://github.com/amforte/Topographic-Analysis-Kit.git>, last access: 13 January 2024 (Forte and Whipple, 2019), respectively.

Data availability. The compilation of data is available in the Supplement.

Supplement. The supplement related to this article is available online at <https://doi.org/10.5194/se-16-503-2025-supplement>.

Author contributions. ZZ: conceptualization, data curation, formal analysis, investigation, methodology, visualization, fieldwork, sample collection, draft writing and revision. TS: data curation, investigation, methodology, validation, project design, regional geology, fieldwork, sample collection, article revision. GW: project administration, funding acquisition, investigation, supervision, fieldwork, article revision. PvdB: data curation, article revision. YZ: data curation, investigation. CM: data curation, investigation.

Competing interests. The contact author has declared that none of the authors has any competing interests.

Disclaimer. Publisher's note: Copernicus Publications remains neutral with regard to jurisdictional claims made in the text, published maps, institutional affiliations, or any other geographical representation in this paper. While Copernicus Publications makes every effort to include appropriate place names, the final responsibility lies with the authors.

Acknowledgements. We sincerely thank Chengyu Zhu and Jie Wei (China University of Geosciences) for their support with fission-track dating and Wei Wang (China University of Geosciences) for assistance during fieldwork. We also appreciate Zhiyuan He (University of Potsdam) for his valuable guidance on article writing and Lingxiao Gong (University of Potsdam) for valuable suggestions on fluvial geomorphic analysis. We are grateful to two anonymous reviewers and Malte Froemchen for their insightful feedback, which greatly improved this paper. We also thank Florian Fousseis for handling this paper.

Financial support. This study was funded by the Key Program of the National Natural Science Foundation of China (grant no. 42430307), the National Natural Science Foundation of China (grant nos. 42172251 and 41972208), and Geological Survey Projects of the China Geological Survey (grant nos. DD20179607 and DD20160060). We gratefully acknowledge the financial support from the China Scholarship Council (CSC; grant no. 202306410183) for funding a research stay of Zihao Zhao in Germany.

Review statement. This paper was edited by Florian Fousseis and reviewed by Malte Froemchen and two anonymous referees.

References

- Allen, M. B. and Vincent, S. J.: Fault reactivation in the Junggar region, northwest China: The role of basement structures during Mesozoic–Cenozoic compression, *J. Geol. Soc.*, 154, 151–155, <https://doi.org/10.1144/gsjgs.154.1.0151>, 1997.
- Allen, M. B., Alsop, G. I., and Zhemchuzhnikov, V. G.: Dome and basin refolding and transpressive inversion along the Karatau Fault System, southern Kazakhstan, *J. Geol. Soc.*, 158, 83–95, <https://doi.org/10.1144/jgs.158.1.83>, 2001.
- Andjic, G., Zhou, R. J., Jonell, T. N., and Aitchison, J. C.: A single Dras–Kohistan–Ladakh Arc revealed by volcanoclastic records, *Geochem. Geophys. Geos.*, 23, 22, <https://doi.org/10.1029/2021gc010042>, 2022.
- Bande, A., Sobel, E. R., Mikolaichuk, A., and Torres Acosta, V.: Talas–Fergana Fault Cenozoic timing of deformation and its relation to Pamir indentation, *Geol. Soc. London Spec. Publ.*, 427, 295, <https://doi.org/10.1144/SP427.1>, 2015.
- Bande, A., Sobel, E. R., Mikolaichuk, A., Schmidt, A., and Stockli, D. F.: Exhumation history of the western Kyrgyz Tien Shan: Implications for intramontane basin formation, *Tectonics*, 36, 163–180, <https://doi.org/10.1002/2016tc004284>, 2017.
- Bazhenov, M. L.: Cretaceous paleomagnetism of the Fergana Basin and adjacent ranges, Central Asia – Tectonic implications, *Tectonophysics*, 221, 251–267, [https://doi.org/10.1016/0040-1951\(93\)90335-h](https://doi.org/10.1016/0040-1951(93)90335-h), 1993.
- Bullen, M. E., Burbank, D. W., Garver, J. I., and Abdrakhmatov, K. Y.: Late Cenozoic tectonic evolution of the northwestern Tien Shan: New age estimates for the initiation of mountain building, *Geol. Soc. Am. Bull.*, 113, 1544–1559, [https://doi.org/10.1130/0016-7606\(2001\)113<1544:Lctect>2.0.Co;2](https://doi.org/10.1130/0016-7606(2001)113<1544:Lctect>2.0.Co;2), 2001.
- Burbank, D. W., McLean, J. K., Bullen, M., Abdrakhmatov, K. Y., and Miller, M. M.: Partitioning of intermontane basins by thrust-related folding, Tien Shan, Kyrgyzstan, *Basin Res.*, 11, 75–92, <https://doi.org/10.1046/j.1365-2117.1999.00086.x>, 1999.
- Burchfiel, B. C., Brown, E. T., Deng, Q. D., Feng, X. Y., Li, J., Molnar, P., Shi, J. B., Wu, Z. M., and You, H. C.: Crustal shortening on the margins of the Tien Shan, Xinjiang, China, *Int. Geol. Rev.*, 41, 665–700, <https://doi.org/10.1080/00206819909465164>, 1999.
- Calvet, M., Gunnell, Y., and Farines, B.: Flat-topped mountain ranges: Their global distribution and value for understanding the evolution of mountain topography, *Geomorphology*, 241, 255–291, <https://doi.org/10.1016/j.geomorph.2015.04.015>, 2015.
- Cao, K., Tian, Y., van der Beek, P., Wang, G., Shen, T., Reiners, P., Bernet, M., and Husson, L.: Southwestward growth of plateau surfaces in eastern Tibet, *Earth-Sci. Rev.*, 232, 104160, <https://doi.org/10.1016/j.earscirev.2022.104160>, 2022.
- Cao, L., Shao, L., Qiao, P., Zhao, Z., and van Hinsbergen, D. J. J.: Early Miocene birth of modern Pearl River recorded low-relief, high-elevation surface formation of SE Tibetan Plateau, *Earth Planet. Sc. Lett.*, 496, 120–131, <https://doi.org/10.1016/j.epsl.2018.05.039>, 2018.
- Chang, J., Li, D., Min, K., Qiu, N. S., Xiao, Y., Wu, H., and Liu, N.: Cenozoic deformation of the Kalpin fold-and-thrust belt, southern Chinese Tian Shan: New insights from low-T thermochronology and sandbox modeling, *Tectonophysics*, 766, 416–432, <https://doi.org/10.1016/j.tecto.2019.06.018>, 2019.
- Charreau, J., Blard, P.-H., Lavé, J., Dominguez, S., and Li, W. S.: Unsteady topography in the eastern Tianshan due to imbalance between denudation and crustal thickening, *Tectonophysics*, 848, 229702, <https://doi.org/10.1016/j.tecto.2022.229702>, 2023.
- Charreau, J., Saint-Carlier, D., Dominguez, S., Lavé, J., Blard, P.-H., Avouac, J.-P., Jolivet, M., Chen, Y., Wang, S., Brown, N. D., Malatesta, L. C., and Rhodes, E.: Denudation outpaced by crustal thickening in the eastern Tianshan, *Earth Planet. Sc. Lett.*, 479, 179–191, <https://doi.org/10.1016/j.epsl.2017.09.025>, 2017.
- Charvet, J., Shu, L. S., Laurent-Charvet, S., Wang, B., Faure, M., Cluzel, D., Chen, Y., and de Jong, K.: Palaeozoic tectonic evolution of the Tianshan belt, NW China, *Sci. China Earth Sci.*, 54, 166–184, <https://doi.org/10.1007/s11430-010-4138-1>, 2011.
- Chen, H. L., Lin, X. B., Cheng, X. G., Gong, J. F., Bian, S., Wu, L., Jia, C. Z., Yang, S. F., Guo, Z. J., and Jia, D.: Two-phase intracontinental deformation mode in the context of India–Eurasia collision: insights from a structural analysis of the West Kunlun–Southern Junggar transect along the NW margin of the Tibetan Plateau, *J. Geol. Soc.*, 179, 14, <https://doi.org/10.1144/jgs2021-029>, 2022.
- Chen, X., Yin, A., Gehrels, G. E., Cowgill, E. S., Grove, M., Harrison, T. M., and Wang, X.: Two phases of Mesozoic north–south extension in the eastern Altyn Tagh range, northern Tibetan Plateau, *Tectonics*, 22, 2001TC001336, <https://doi.org/10.1029/2001TC001336>, 2003.
- Chen, Y., Wang, G. C., Zhao, X., Wang, Y. B., Ji, J. L., Cao, K., Shen, T. Y., Zhang, P., and Wang, A.: Evolution of the Barkol Basin, eastern Tian Shan, and its geodynamic background, *Int. J. Earth Sci.*, 108, 1253–1271, <https://doi.org/10.1007/s00531-019-01704-y>, 2019.
- Chen, Y., Wang, G. C., Kapp, P., Shen, T. Y., Zhang, P., Zhu, C. Y., and Cao, K.: Episodic exhumation and related tec-

- tonic controlling during Mesozoic in the Eastern Tian Shan, Xinjiang, northwestern China, *Tectonophysics*, 796, 228647, <https://doi.org/10.1016/j.tecto.2020.228647>, 2020a.
- Chen, Y., Wang, G. C., Shen, T. Y., Zhang, P., Sotiriou, P., and Zhu, C. Y.: Tectono-geomorphic evolution of Harlik Mountain in the Eastern Tian Shan, insight from thermochronological data and geomorphic analysis, *Geol. J.*, 55, 7322–7334, <https://doi.org/10.1002/gj.3951>, 2020b.
- Chen, Z. L., Wang, Z. X., Han, F. B., Zhang, W. G., Zhang, Q., Zhou, Z. J., Wang, X. H., Xiao, W. F., Han, S. Q., Yu, X. Q., Sun, Y., Nurgazy, T., Latyshev, N., and Zailabidin, H.: Late Cretaceous-Cenozoic uplift, deformation, and erosion of the SW Tianshan Mountains in Kyrgyzstan and Western China, *Int. Geol. Rev.*, 60, 1019–1037, <https://doi.org/10.1080/00206814.2017.1365018>, 2018.
- China Geological Survey: Geological map of Chinese Tianshan and adjacent areas, scale 1 : 1 000 000, Xi'an Institute of Geology and Mineral Resource, Xi'an, China, Geological Publishing House, GS(2006)463, 2007.
- Clark, M. K., Royden, L. H., Whipple, K. X., Burchfiel, B. C., Zhang, X., and Tang, W.: Use of a regional, relict landscape to measure vertical deformation of the eastern Tibetan Plateau, *J. Geophys. Res.-Earth*, 111, F03002, <https://doi.org/10.1029/2005JF000294>, 2006.
- Cunningham, D.: Structural and topographic characteristics of restraining bend mountain ranges of the Altai, Gobi Altai and easternmost Tien Shan, *Geol. Soc. London Spec. Publ.*, 290, 219, <https://doi.org/10.1144/SP290.7>, 2007.
- Cunningham, D.: Mountain building processes in intracontinental oblique deformation belts: Lessons from the Gobi Corridor, Central Asia, *J. Struct. Geol.*, 46, 255–282, <https://doi.org/10.1016/j.jsg.2012.08.010>, 2013.
- Cunningham, D. and Zhang, J.: China | Mongolia: Mesozoic–Cenozoic, *Encyclopedia of Geology*, 509–525, <https://doi.org/10.1016/b978-0-08-102908-4.00164-8>, 2021.
- Cunningham, D., Owen, L. A., Snee, L. W., and Li, J. L.: Structural framework of a major intracontinental orogenic termination zone: the easternmost Tien Shan, China, *J. Geol. Soc.*, 160, 575–590, <https://doi.org/10.1144/0016-764902-122>, 2003.
- De Grave, J. and Van den Haute, P.: Denudation and cooling of the Lake Teletskoye Region in the Altai Mountains (South Siberia) as revealed by apatite fission-track thermochronology, *Tectonophysics*, 349, 145–159, [https://doi.org/10.1016/s0040-1951\(02\)00051-3](https://doi.org/10.1016/s0040-1951(02)00051-3), 2002.
- De Grave, J., Buslov, M. M., and Van den Haute, P.: Distant effects of India–Eurasia convergence and Mesozoic intracontinental deformation in Central Asia: Constraints from apatite fission-track thermochronology, *J. Asian Earth Sci.*, 29, 188–204, <https://doi.org/10.1016/j.jseae.2006.03.001>, 2007.
- De Grave, J., Van den Haute, P., Buslov, M. M., Dehandschutter, B., and Glorie, S.: Apatite fission-track thermochronology applied to the Chulyshman Plateau, Siberian Altai Region, *Radiat. Meas.*, 43, 38–42, <https://doi.org/10.1016/j.radmeas.2007.11.068>, 2008.
- De Grave, J., Glorie, S., Buslov, M. M., Izmer, A., Fournier-Carrie, A., Batalev, V. Y., Vanhaecke, F., Elburg, M., and Van den Haute, P.: The thermo-tectonic history of the Song-Kul plateau, Kyrgyz Tien Shan: Constraints by apatite and titanite thermochronometry and zircon U/Pb dating, *Gondwana Res.*, 20, 745–763, <https://doi.org/10.1016/j.gr.2011.03.011>, 2011.
- De Grave, J., Glorie, S., Ryabinin, A., Zhimulev, F., Buslov, M. M., Izmer, A., Elburg, M., Vanhaecke, F., and Van den Haute, P.: Late Palaeozoic and Meso-Cenozoic tectonic evolution of the southern Kyrgyz Tien Shan: Constraints from multi-method thermochronology in the Trans-Alai, Turkestan-Alai segment and the southeastern Ferghana Basin, *J. Asian Earth Sci.*, 44, 149–168, <https://doi.org/10.1016/j.jseae.2011.04.019>, 2012.
- De Grave, J., Glorie, S., Buslov, M. M., Stockli, D. F., McWilliams, M. O., Batalev, V. Y., and Van den Haute, P.: Thermo-tectonic history of the Issyk-Kul basement (Kyrgyz Northern Tien Shan, Central Asia), *Gondwana Res.*, 23, 998–1020, <https://doi.org/10.1016/j.gr.2012.06.014>, 2013.
- De Grave, J., De Pelsmaeker, E., Zhimulev, F. I., Glorie, S., Buslov, M. M., and Van den Haute, P.: Meso-Cenozoic building of the northern Central Asian Orogenic Belt: Thermotectonic history of the Tuva region, *Tectonophysics*, 621, 44–59, <https://doi.org/10.1016/j.tecto.2014.01.039>, 2014.
- De Pelsmaeker, E., Glorie, S., Buslov, M. M., Zhimulev, F. I., Poujol, M., Korobkin, V. V., Vanhaecke, F., Vetrov, E. V., and De Grave, J.: Late-Paleozoic emplacement and Meso-Cenozoic reactivation of the southern Kazakhstan granitoid basement, *Tectonophysics*, 662, 416–433, <https://doi.org/10.1016/j.tecto.2015.06.014>, 2015.
- De Pelsmaeker, E., Jolivet, M., Laborde, A., Poujol, M., Robin, C., Zhimulev, F. I., Nachtergaele, S., Glorie, S., De Clercq, S., Batalev, V. Y., and De Grave, J.: Source-to-sink dynamics in the Kyrgyz Tien Shan from the Jurassic to the Paleogene: Insights from sedimentological and detrital zircon U–Pb analyses, *Gondwana Res.*, 54, 180–204, <https://doi.org/10.1016/j.gr.2017.09.004>, 2018.
- Delvaux, D. and Sperner, B.: New aspects of tectonic stress inversion with reference to the TENSOR program, *Geol. Soc. London Spec. Publ.*, 212, 75, <https://doi.org/10.1144/GSL.SP.2003.212.01.06>, 2003.
- Deng, X.-H., Wang, J.-B., Pirajino, F., Wang, Y.-W., Li, Y.-C., Li, C., Zhou, L.-M., and Chen, Y.-J.: Re–Os dating of chalcopyrite from selected mineral deposits in the Kalatag district in the eastern Tianshan Orogen, China, *Ore Geol. Rev.*, 77, 72–81, <https://doi.org/10.1016/j.oregeorev.2016.01.014>, 2016.
- Ding, L., Kapp, P., Cai, F., Garzzone, C. N., Xiong, Z., Wang, H., and Wang, C.: Timing and mechanisms of Tibetan Plateau uplift, *Nat. Rev. Earth Environ.*, 3, 652–667, <https://doi.org/10.1038/s43017-022-00318-4>, 2022.
- Ding, Y., Shen, T., Wang, G., and Ji, J.: Sedimentary and heavy mineral records for the Oligocene–Miocene exhumation of the easternmost Tianshan, *J. Earth Sci.*, 35, 449–461, <https://doi.org/10.1007/s12583-022-1757-3>, 2024.
- Donskaya, T. V., Windley, B. F., Mazukabzov, A. M., Kroener, A., Sklyarov, E. V., Gladkochub, D. P., Ponomarchuk, V. A., Badarch, G., Reichow, M. K., and Hegner, E.: Age and evolution of late Mesozoic metamorphic core complexes in southern Siberia and northern Mongolia, *J. Geol. Soc.*, 165, 405–421, <https://doi.org/10.1144/0016-76492006-162>, 2008.
- Dumitru, T. A., Da, Z., Chang, E. Z., Graham, S. A., and Carroll, A. R.: Uplift, exhumation, and deformation in the Chinese Tian Shan, *Geol. Soc. Am. Mem.*, 194, 71–99, 2001.
- Eberth, D. A., Brinkman, D. B., Chen, P.-J., Yuan, F.-T., Wu, S.-Z., Li, G., and Cheng, X.-S.: Sequence stratigraphy, paleoclimate patterns, and vertebrate fossil preservation in Jurassic-

- Cretaceous strata of the Junggar Basin, Xinjiang Autonomous Region, People's Republic of China, *Can. J. Earth Sci.*, 38, 1627–1644, <https://doi.org/10.1139/e01-067>, 2001.
- England, P. and Molnar, P.: Surface uplift, uplift of rocks, and exhumation of rocks, *Geology*, 18, 1173–1177, [https://doi.org/10.1130/0091-7613\(1990\)018<1173:suora>2.3.co;2](https://doi.org/10.1130/0091-7613(1990)018<1173:suora>2.3.co;2), 1990.
- Flint, J. J.: Stream gradient as a function of order, magnitude, and discharge, *Water Resour. Res.*, 10, 969–973, <https://doi.org/10.1029/WR010i005p00969>, 1974.
- Forte, A. M. and Whipple, K. X.: Short communication: The Topographic Analysis Kit (TAK) for TopoToolbox, *Earth Surf. Dynam.*, 7, 87–95, <https://doi.org/10.5194/esurf-7-87-2019>, 2019.
- Gaillon, B., Mudd, S. M., Clubb, F. J., Grieve, S. W. D., and Hurst, M. D.: Impact of changing concavity indices on channel steepness and divide migration metrics, *J. Geophys. Res.-Earth*, 126, e2020JF006060, <https://doi.org/10.1029/2020JF006060>, 2021.
- Galbraith, R. F. and Laslett, G. M.: Statistical models for mixed fission track ages, *Nucl. Tracks Rad. Meas.*, 21, 459–470, [https://doi.org/10.1016/1359-0189\(93\)90185-C](https://doi.org/10.1016/1359-0189(93)90185-C), 1993.
- Gallagher, K.: Transdimensional inverse thermal history modeling for quantitative thermochronology, *J. Geophys. Res.-Sol. Ea.*, 117, 16, <https://doi.org/10.1029/2011jb008825>, 2012.
- Gao, H. L., Liu, G. X., He, J. G., Tian, M. M., and Che, Y. F.: Mesozoic–Cenozoic uplift exhumation history of East Tianshan: Evidence from apatite fission track, *Earth Sci. Front.*, 21, 249–260 (in Chinese with English abstract), 2014.
- Gillespie, J., Glorie, S., Jepson, G., Zhang, Z. Y., Xiao, W. J., Danisik, M., and Collins, A. S.: Differential exhumation and crustal tilting in the easternmost Tianshan (Xinjiang, China), revealed by low-temperature thermochronology, *Tectonics*, 36, 2142–2158, <https://doi.org/10.1002/2017tc004574>, 2017a.
- Gillespie, J., Glorie, S., Xiao, W. J., Zhang, Z. Y., Collins, A. S., Evans, N., McInnes, B., and De Grave, J.: Mesozoic reactivation of the Beishan, southern Central Asian Orogenic Belt: Insights from low-temperature thermochronology, *Gondwana Res.*, 43, 107–122, <https://doi.org/10.1016/j.gr.2015.10.004>, 2017b.
- Gillespie, J., Glorie, S., Jepson, G., Zhimulev, F., Gurevich, D., Danisik, M., and Collins, A. S.: Inherited structure as a control on late Paleozoic and Mesozoic exhumation of the Tarbagatai Mountains, southeastern Kazakhstan, *J. Geol. Soc.*, <https://doi.org/10.1144/jgs2020-121>, 2021.
- Gleadow, A. J. W., Belton, D. X., Kohn, B. P., and Brown, R. W.: Fission-track dating of phosphate minerals and the thermochronology of apatite, *Rev. Min. Geochem.*, 48, 579–630, <https://doi.org/10.2138/rmg.2002.48.16>, 2002.
- Glorie, S. and De Grave, J.: Exhuming the Meso-Cenozoic Kyrgyz Tianshan and Siberian Altai-Sayan: A review based on low-temperature thermochronology, *Geosci. Front.*, 7, 155–170, <https://doi.org/10.1016/j.gsf.2015.04.003>, 2016.
- Glorie, S., De Grave, J., Buslov, M. M., Elburg, M. A., Stockli, D. F., Gerdes, A., and Van den Haute, P.: Multi-method chronometric constraints on the evolution of the Northern Kyrgyz Tien Shan granitoids (Central Asian Orogenic Belt): From emplacement to exhumation, *J. Asian Earth Sci.*, 38, 131–146, <https://doi.org/10.1016/j.jseaes.2009.12.009>, 2010.
- Glorie, S., De Grave, J., Buslov, M. M., Zhimulev, F. I., Stockli, D. F., Batalev, V. Y., Izmer, A., Van den Haute, P., Vanhaecke, F., and Elburg, M. A.: Tectonic history of the Kyrgyz South Tien Shan (Atbashi–Inylchek) suture zone: The role of inherited structures during deformation-propagation, *Tectonics*, 30, TC6016, <https://doi.org/10.1029/2011tc002949>, 2011.
- Glorie, S., De Grave, J., Buslov, M. M., Zhimulev, F. I., Elburg, M. A., and Van den Haute, P.: Structural control on Meso-Cenozoic tectonic reactivation and denudation in the Siberian Altai: Insights from multi-method thermochronometry, *Tectonophysics*, 544, 75–92, <https://doi.org/10.1016/j.tecto.2012.03.035>, 2012a.
- Glorie, S., De Grave, J., Delvaux, D., Buslov, M. M., Zhimulev, F. I., Vanhaecke, F., Elburg, M. A., and Van den Haute, P.: Tectonic history of the Irtysh shear zone (NE Kazakhstan): New constraints from zircon U/Pb dating, apatite fission track dating and palaeostress analysis, *J. Asian Earth Sci.*, 45, 138–149, <https://doi.org/10.1016/j.jseaes.2011.09.024>, 2012b.
- Glorie, S., Otasevic, A., Gillespie, J., Jepson, G., Danisik, M., Zhimulev, F. I., Gurevich, D., Zhang, Z., Song, D., and Xiao, W.: Thermo-tectonic history of the Junggar Alatau within the Central Asian Orogenic Belt (SE Kazakhstan, NW China): Insights from integrated apatite U/Pb, fission track and (U–Th)/He thermochronology, *Geosci. Front.*, 10, 2153–2166, <https://doi.org/10.1016/j.gsf.2019.05.005>, 2019.
- Glorie, S., Nixon, A. L., Jepson, G., Gillespie, J., Warren, C., Meeuws, F., Simpson, A., and Xiao, W.: Meso-Cenozoic tectonic history of the Altai: New insights from apatite U–Pb and fission track thermochronology for the Fuyun Area (Xinjiang, China), *Tectonics*, 42, e2022TC007692, <https://doi.org/10.1029/2022TC007692>, 2023.
- Gong, L., Kohn, B. P., Zhang, Z. Y., Xiao, B., Wu, L., and Chen, H. Y.: Exhumation and preservation of Paleozoic porphyry Cu deposits: Insights from the Yandong Deposit, southern Central Asian Orogenic Belt, *Econ. Geol.*, 116, 607–627, <https://doi.org/10.5382/econgeo.4812>, 2021.
- Gong, L., van der Beek, P., Schildgen, T. F., Sobel, E. R., Racano, S., Mariotti, A., and McNab, F.: Drainage rearrangement in an intra-continental mountain belt: a case study from the central South Tian Shan, Kyrgyzstan, *Earth Surf. Dynam.*, 12, 973–994, <https://doi.org/10.5194/esurf-12-973-2024>, 2024.
- Graham, S. A., Hendrix, M. S., Johnson, C. L., Badamgarav, D., Badarch, G., Amory, J., Porter, M., Barsbold, R., Webb, L. E., and Hacker, B. R.: Sedimentary record and tectonic implications of Mesozoic rifting in southeast Mongolia, *Geol. Soc. Am. Bull.*, 113, 1560–1579, [https://doi.org/10.1130/0016-7606\(2001\)113<1560:Sratio>2.0.Co;2](https://doi.org/10.1130/0016-7606(2001)113<1560:Sratio>2.0.Co;2), 2001.
- Guan, X. T., Wu, C. D., Zhou, T. Q., Tang, X. Y., Ma, J., and Fang, Y. N.: Jurassic-Lower Cretaceous sequence stratigraphy and allogenic controls in proximal terrestrial environments (Southern Junggar Basin, NW China), *Geol. J.*, 56, 4038–4062, <https://doi.org/10.1002/gj.4132>, 2021.
- Haider, V. L., Kropacek, J., Dunkl, I., Wagner, B., and von Eynatten, H.: Identification of penneplains by multi-parameter assessment of digital elevation models, *Earth Surf. Proc. Land.*, 40, 1477–1492, <https://doi.org/10.1002/esp.3729>, 2015.
- Hasebe, N., Barbarand, J., Jarvis, K., Carter, A., and Hurford, A. J.: Apatite fission-track chronometry using laser ablation ICP-MS, *Chem. Geol.*, 207, 135–145, <https://doi.org/10.1016/j.chemgeo.2004.01.007>, 2004.

- Hasebe, N., Tamura, A., and Arai, S.: Zeta equivalent fission-track dating using LA-ICP-MS and examples with simultaneous U–Pb dating, *Isl. Arc*, 22, 280–291, <https://doi.org/10.1111/iar.12040>, 2013.
- He, Z., Wang, B., Ni, X., De Grave, J., Scaillet, S., Chen, Y., Liu, J., and Zhu, X.: Structural and kinematic evolution of strike-slip shear zones around and in the central Tianshan: Insights for eastward tectonic wedging in the southwest Central Asian Orogenic Belt, *J. Struct. Geol.*, 144, 104279, <https://doi.org/10.1016/j.jsg.2021.104279>, 2021a.
- He, Z., Wang, B., Glorie, S., Su, W., Ni, X., Jepson, G., Liu, J., Zhong, L., Gillespie, J., and De Grave, J.: Mesozoic building of the Eastern Tianshan and East Junggar (NW China) revealed by low-temperature thermochronology, *Gondwana Res.*, 103, 37–53, <https://doi.org/10.1016/j.gr.2021.11.013>, 2022a.
- He, Z., Glorie, S., Wang, F., Zhu, W., Fonseca, A., Su, W., Zhong, L., Zhu, X., and De Grave, J.: A re-evaluation of the Meso–Cenozoic thermo-tectonic evolution of Bogda Shan (Tian Shan, NW China) based on new basement and detrital apatite fission track thermochronology, *Int. Geol. Rev.*, 65, 2093–2112, <https://doi.org/10.1080/00206814.2022.2121946>, 2023.
- He, Z., Song, S., Wang, F., Zhu, W., Shen, X., Glorie, S., Liang, Y., Zhong, L., and De Grave, J.: Late Mesozoic intra-continental reactivation of the southern Altai, central Asia, *Geol. Soc. Am. Bull.*, 137, 2287–2302, <https://doi.org/10.1130/B37905.1>, 2024.
- He, Z. Y., Wang, B., Nachtergaele, S., Glorie, S., Ni, X., Su, W., Cai, D., Liu, J., and De Grave, J.: Long-term topographic evolution of the Central Tianshan (NW China) constrained by low-temperature thermochronology, *Tectonophysics*, 817, 229066, <https://doi.org/10.1016/j.tecto.2021.229066>, 2021b.
- He, Z. Y., Wang, B., Su, W. B., Glorie, S., Ni, X. H., Liu, J. S., Cai, D. X., Zhong, L. L., and De Grave, J.: Meso-Cenozoic thermo-tectonic evolution of the Yili block within the Central Asian Orogenic Belt (NW China): Insights from apatite fission track thermochronology, *Tectonophysics*, 823, 17, <https://doi.org/10.1016/j.tecto.2021.229194>, 2022b.
- Hendrix, M. S., Graham, S. A., Carroll, A. R., Sobel, E. R., McKnight, C. L., Schulein, B. J., and Wang, Z. X.: Sedimentary record and climatic implications of recurrent deformation in the Tian-Shan – evidence from Mesozoic strata of the north Tarim, south Junggar, and Turpan basins, northwest China, *Geol. Soc. Am. Bull.*, 104, 53–79, [https://doi.org/10.1130/0016-7606\(1992\)104<0053:Scracio>2.3.Co;2](https://doi.org/10.1130/0016-7606(1992)104<0053:Scracio>2.3.Co;2), 1992.
- Hetzel, R., Dunkl, I., Haider, V., Strobl, M., von Eynatten, H., Ding, L., and Frei, D.: Peneplain formation in southern Tibet predates the India-Asia collision and plateau uplift, *Geology*, 39, 983–986, <https://doi.org/10.1130/g32069.1>, 2011.
- Hu, X., Ma, A., Xue, W., Garzanti, E., Cao, Y., Li, S.-M., Sun, G., and Lai, W.: Exploring a lost ocean in the Tibetan Plateau: Birth, growth, and demise of the Bangong-Nujiang Ocean, *Earth-Sci. Rev.*, 229, 104031, <https://doi.org/10.1016/j.earscirev.2022.104031>, 2022.
- Hui, J., Cheng, H., Zhang, J., Zhang, K., Qu, J., and Zhang, B.: Early cretaceous continent basalts in the Alxa block, NW China: Geochronology, geochemistry, and tectonic implications, *Int. Geol. Rev.*, 63, 882–899, <https://doi.org/10.1080/00206814.2020.1734974>, 2021.
- Jaiswara, N. K., Pandey, P., and Pandey, A. K.: Mio-Pliocene piracy, relict landscape and drainage reorganization in the Namcha Barwa syntaxis zone of eastern Himalaya, *Sci. Rep.*, 9, 17585, <https://doi.org/10.1038/s41598-019-54052-x>, 2019.
- Jepson, G., Glorie, S., Konopelko, D., Gillespie, J., Danisik, M., Mirkamalov, R., Mamadjanov, Y., and Collins, A. S.: Low-temperature thermochronology of the Chatkal-Kurama terrane (Uzbekistan-Tajikistan): Insights into the Meso-Cenozoic thermal history of the Western Tian Shan, *Tectonics*, 37, 3954–3969, <https://doi.org/10.1029/2017tc004878>, 2018a.
- Jepson, G., Glorie, S., Konopelko, D., Mirkamalov, R., Danisik, M., and Collins, A. S.: The low-temperature thermo-tectonic evolution of the western Tian Shan, *Uzbekistan, Gondwana Res.*, 64, 122–136, <https://doi.org/10.1016/j.gr.2018.08.003>, 2018b.
- Jepson, G., Glorie, S., Konopelko, D., Gillespie, J., Danisik, M., Evans, N. J., Mamadjanov, Y., and Collins, A. S.: Thermochronological insights into the structural contact between the Tian Shan and Pamirs, *Tajikistan, Terra Nova*, 30, 95–104, <https://doi.org/10.1111/ter.12313>, 2018c.
- Jepson, G., Carrapa, B., Gillespie, J., Feng, R., DeCelles, P. G., Kapp, P., Tabor, C. R., and Zhu, J.: Climate as the great equalizer of continental-scale erosion, *Geophys. Res. Lett.*, 48, e2021GL095008, <https://doi.org/10.1029/2021GL095008>, 2021a.
- Jepson, G., Glorie, S., Khudoley, A. K., Malyshev, S. V., Gillespie, J., Glasmacher, U. A., Carrapa, B., Soloviev, A. V., and Collins, A. S.: The Mesozoic exhumation history of the Karatau-Talas range, western Tian Shan, *Kazakhstan–Kyrgyzstan, Tectonophysics*, 814, 228977, <https://doi.org/10.1016/j.tecto.2021.228977>, 2021b.
- Ji, H. J., Tao, H. F., Wang, Q., Ma, D. X., and Hao, L. W.: Petrography, geochemistry, and geochronology of Lower Jurassic sedimentary rocks from the Northern Tianshan (West Bogda area), Northwest China: Implications for provenance and tectonic evolution, *Geol. J.*, 54, 1688–1714, <https://doi.org/10.1002/gj.3263>, 2019.
- Jia, Y. Y., Fu, B. H., Jolivet, M., and Zheng, S.: Cenozoic tectono-geomorphological growth of the SW Chinese Tian Shan: Insight from AFT and detrital zircon U–Pb data, *J. Asian Earth Sci.*, 111, 395–413, <https://doi.org/10.1016/j.jseaes.2015.06.023>, 2015.
- Jiang, Y., Lu, H., Yang, R., Pang, L., Jiao, R., Wang, Y., Pang, J., and Li, Y.: Two-stage exhumation, uplift, and basinward propagation of the Tian Shan during the late Cenozoic, *Earth-Sci. Rev.*, 256, 104868, <https://doi.org/10.1016/j.earscirev.2024.104868>, 2024.
- Jolivet, M.: Mesozoic tectonic and topographic evolution of Central Asia and Tibet: a preliminary synthesis, *Geol. Soc. London Spec. Publ.*, 427, 19–55, <https://doi.org/10.1144/SP427.2>, 2017.
- Jolivet, M., Ritz, J. F., Vassallo, R., Larroque, C., Braucher, R., Todbileg, M., Chauvet, A., Sue, C., Arnaud, N., De Vicente, R., Arzhanikova, A., and Arzhanikov, S.: Mongolian summits: An uplifted, flat, old but still preserved erosion surface, *Geology*, 35, 871–874, <https://doi.org/10.1130/g23758a.1>, 2007.
- Jolivet, M., De Boisgrollier, T., Petit, C., Fournier, M., Sankov, V. A., Ringenbach, J. C., Byzov, L., Miroshnichenko, A. I., Kovalenko, S. N., and Anisimova, S. V.: How old is the Baikal Rift Zone? Insight from apatite fission track thermochronology, *Tectonics*, 28, 21, <https://doi.org/10.1029/2008tc002404>, 2009.
- Jolivet, M., Dominguez, S., Charreau, J., Chen, Y., Li, Y. G., and Wang, Q. C.: Mesozoic and Cenozoic tectonic history of the central Chinese Tian Shan: Reactivated tectonic

- structures and active deformation, *Tectonics*, 29, TC6019, <https://doi.org/10.1029/2010tc002712>, 2010.
- Jolivet, M., Barrier, L., Dauteuil, O., Laborde, A., Li, Q., Reichenbacher, B., Popescu, S. M., Sha, J. G., and Guo, Z. J.: Late Cretaceous–Palaeogene topography of the Chinese Tian Shan: New insights from geomorphology and sedimentology, *Earth Planet. Sc. Lett.*, 499, 95–106, <https://doi.org/10.1016/j.epsl.2018.07.004>, 2018.
- Kapp, P., DeCelles, P. G., Gehrels, G. E., Heizler, M., and Ding, L.: Geological records of the Lhasa–Qiangtang and Indo-Asian collisions in the Nima area of central Tibet, *Geol. Soc. Am. Bull.*, 119, 917–932, <https://doi.org/10.1130/B26033.1>, 2007.
- Kassner, A., Ratschbacher, L., Jonckheere, R., Enkelmann, E., Khan, J., Sonntag, B. L., Gloaguen, R., Gadoev, M., and Oimahmadov, I.: Cenozoic intracontinental deformation and exhumation at the northwestern tip of the India–Asia collision, southwestern Tian Shan, Tajikistan and Kyrgyzstan, *Tectonics*, 35, 2171–2194, <https://doi.org/10.1002/2015tc003897>, 2016.
- Ketcham, R. A., Carter, A., Donelick, R. A., Barbarand, J., and Hurford, A. J.: Improved modeling of fission-track annealing in apatite, *Am. Mineral.*, 92, 799–810, <https://doi.org/10.2138/am.2007.2281>, 2007.
- Kirby, E. and Whipple, K.: Quantifying differential rock-uplift rates via stream profile analysis, *Geology*, 29, 415–418, [https://doi.org/10.1130/0091-7613\(2001\)029<0415:QDRURV>2.0.CO;2](https://doi.org/10.1130/0091-7613(2001)029<0415:QDRURV>2.0.CO;2), 2001.
- Kirby, E. and Whipple, K. X.: Expression of active tectonics in erosional landscapes, *J. Struct. Geol.*, 44, 54–75, <https://doi.org/10.1016/j.jsg.2012.07.009>, 2012.
- Lague, D.: The stream power river incision model: Evidence, theory and beyond, *Earth Surf. Proc. Land.*, 39, 38–61, <https://doi.org/10.1002/esp.3462>, 2014.
- Lai, W., Hu, X. M., Garzanti, E., Xu, Y. W., Ma, A. L., and Li, W.: Early Cretaceous sedimentary evolution of the northern Lhasa terrane and the timing of initial Lhasa–Qiangtang collision, *Gondwana Res.*, 73, 136–152, <https://doi.org/10.1016/j.gr.2019.03.016>, 2019.
- Li, S., Guilmette, C., Ding, L., Xu, Q., Fu, J. J., and Yue, Y. H.: Provenance of Mesozoic clastic rocks within the Bangong–Nujiang suture zone, central Tibet: Implications for the age of the initial Lhasa–Qiangtang collision, *J. Asian Earth Sci.*, 147, 469–484, <https://doi.org/10.1016/j.jseaes.2017.08.019>, 2017.
- Liu, D.-L., Shi, R.-D., Ding, L., and Zou, H.-B.: Late Cretaceous transition from subduction to collision along the Bangong–Nujiang Tethys: New volcanic constraints from central Tibet, *Lithos*, 296–299, 452–470, <https://doi.org/10.1016/j.lithos.2017.11.012>, 2018.
- Liu, F. L., Gao, H. S., Pan, B. T., Li, Z. M., and Su, H.: Quantitative analysis of planation surfaces of the upper Yangtze River in the Sichuan–Yunnan Region, Southwest China, *Front. Earth Sci.*, 13, 55–74, <https://doi.org/10.1007/s11707-018-0707-y>, 2019.
- Liu, K., Chen, X., Zuzza, A., Shao, Z., Qin, X., Han, L., Zhang, Y., Yu, W., Wang, Z., Shi, X., Li, B., and Wang, Y.: The Late Mesozoic intracontinental contraction–extension transition in the Beishan Fold–Thrust Belt, Central Asia: Constraints from structural analysis and apatite (U–Th)/He thermochronology, *Tectonics*, 42, e2022TC007532, <https://doi.org/10.1029/2022TC007532>, 2023.
- Liu–Zeng, J., Tapponnier, P., Gaudemer, Y., and Ding, L.: Quantifying landscape differences across the Tibetan plateau: Implications for topographic relief evolution, *J. Geophys. Res.*, 113, 2007JF000897, <https://doi.org/10.1029/2007JF000897>, 2008.
- Lu, H. H., Chang, Y. A., Wang, W., and Zhou, Z. Y.: Rapid exhumation of the Tianshan Mountains since the early Miocene: Evidence from combined apatite fission track and (U–Th)/He thermochronology, *Sci. China Earth Sci.*, 56, 2116–2125, <https://doi.org/10.1007/s11430-013-4715-1>, 2013.
- Ma, A., Hu, X., Garzanti, E., Han, Z., and Lai, W.: Sedimentary and tectonic evolution of the southern Qiangtang basin: Implications for the Lhasa–Qiangtang collision timing, *J. Geophys. Res.–Sol. Ea.*, 122, 4790–4813, <https://doi.org/10.1002/2017JB014211>, 2017.
- Ma, X. X., Shu, L. S., and Meert, J. G.: Early Permian slab breakoff in the Chinese Tianshan belt inferred from the post-collisional granitoids, *Gondwana Res.*, 27, 228–243, <https://doi.org/10.1016/j.gr.2013.09.018>, 2015.
- Macaulay, E. A., Sobel, E. R., Mikolaichuk, A., Kohn, B., and Stuart, F. M.: Cenozoic deformation and exhumation history of the Central Kyrgyz Tien Shan, *Tectonics*, 33, 135–165, <https://doi.org/10.1002/2013tc003376>, 2014.
- Marrucci, M., Zeilinger, G., Ribolini, A., and Schwanghart, W.: Origin of knickpoints in an alpine context subject to different perturbing factors, Stura valley, Maritime Alps (north-western Italy), *Geoscience*, 8, 443, <https://doi.org/10.3390/geosciences8120443>, 2018.
- Meng, Q.-R.: What drove late Mesozoic extension of the northern China–Mongolia tract?, *Tectonophysics*, 369, 155–174, [https://doi.org/10.1016/S0040-1951\(03\)00195-1](https://doi.org/10.1016/S0040-1951(03)00195-1), 2003.
- Molnar, P. and Tapponnier, P.: Cenozoic tectonics of Asia: Effects of a continental collision, *Science*, 189, 419–426, <https://doi.org/10.1126/science.189.4201.419>, 1975.
- Morin, J., Jolivet, M., Barrier, L., Laborde, A., Li, H. B., and Dauteuil, O.: Planation surfaces of the Tian Shan Range (Central Asia): Insight on several 100 million years of topographic evolution, *J. Asian Earth Sci.*, 177, 52–65, <https://doi.org/10.1016/j.jseaes.2019.03.011>, 2019.
- Nachtergaele, S., De Pelsmaeker, E., Glorie, S., Zhimulev, F., Jolivet, M., Danisik, M., Buslov, M. M., and De Grave, J.: Meso–Cenozoic tectonic evolution of the Talas–Fergana region of the Kyrgyz Tien Shan revealed by low-temperature basement and detrital thermochronology, *Geosci. Front.*, 9, 1495–1514, <https://doi.org/10.1016/j.gsf.2017.11.007>, 2018.
- Ni, X., Wang, B., Cluzel, D., Liu, J., and He, Z.: Late Paleozoic tectonic evolution of the north Tianshan belt: New structural and geochronological constraints from meta-sedimentary rocks and migmatites in the Harlik range (NW China), *J. Asian Earth Sci.*, 210, 104711, <https://doi.org/10.1016/j.jseaes.2021.104711>, 2021.
- Pearce, N. J. G., Perkins, W. T., Westgate, J. A., Gorton, M. P., Jackson, S. E., Neal, C. R., and Chenery, S. P.: A compilation of new and published major and trace element data for NIST SRM 610 and NIST SRM 612 glass reference materials, *Geo-standard Newslett.*, 21, 115–144, <https://doi.org/10.1111/j.1751-908X.1997.tb00538.x>, 1997.
- Phillips, J. D.: Erosion, isostatic response, and the missing peneplains, *Geomorphology*, 45, 225–241, [https://doi.org/10.1016/S0169-555x\(01\)00156-8](https://doi.org/10.1016/S0169-555x(01)00156-8), 2002.

- Pullen, A., Banaszynski, M., Kapp, P., Thomson, S. N., and Cai, F.: A mid-Cretaceous change from fast to slow exhumation of the western Chinese Altai mountains: A climate driven exhumation signal?, *J. Asian Earth Sci.*, 197, 104387, <https://doi.org/10.1016/j.jseaes.2020.104387>, 2020.
- Qin, Y., Liu, C. Y., Yang, L. H., Peng, H., and Jiao, X. Q.: Detrital-zircon geochronology of Jurassic-Cretaceous strata in the Turpan-Hami Basin: Implication for the Late Mesozoic tectonic evolution of eastern Tien Shan, *Minerals*, 12, 926, <https://doi.org/10.3390/min12080926>, 2022.
- Rohrmann, A., Kapp, P., Carrapa, B., Reiners, P. W., Guynn, J., Ding, L., and Heizler, M.: Thermochronologic evidence for plateau formation in central Tibet by 45 Ma, *Geology*, 40, 187–190, <https://doi.org/10.1130/G32530.1>, 2012.
- Rolland, Y., Jourdon, A., Petit, C., Bellahsen, N., Loury, C., Sobel, E. R., and Glodny, J.: Thermochronology of the highest central Asian massifs (Khan Tengri-Pobedi, SE Kyrgyzstan): Evidence for Late Miocene (ca. 8 Ma) reactivation of Permian faults and insights into building the Tian Shan, *J. Asian Earth Sci.*, 200, 104466, <https://doi.org/10.1016/j.jseaes.2020.104466>, 2020.
- Schwab, M., Ratschbacher, L., Siebel, W., McWilliams, M., Minaev, V., Lutkov, V., Chen, F. K., Stanek, K., Nelson, B., Frisch, W., and Wooden, J. L.: Assembly of the Pamirs: Age and origin of magmatic belts from the southern Tien Shan to the southern Pamirs and their relation to Tibet, *Tectonics*, 23, TC4002, <https://doi.org/10.1029/2003tc001583>, 2004.
- Schwanghart, W. and Scherler, D.: Short Communication: Topo-Toolbox 2 – MATLAB-based software for topographic analysis and modeling in Earth surface sciences, *Earth Surf. Dynam.*, 2, 1–7, <https://doi.org/10.5194/esurf-2-1-2014>, 2014.
- Schwanghart, W. and Scherler, D.: Bumps in river profiles: uncertainty assessment and smoothing using quantile regression techniques, *Earth Surf. Dynam.*, 5, 821–839, <https://doi.org/10.5194/esurf-5-821-2017>, 2017.
- Shao, L., Statterger, K., Li, W., and Haupt, B. J.: Depositional style and subsidence history of the Turpan Basin (NW China), *Sed. Geol.*, 128, 155–169, [https://doi.org/10.1016/S0037-0738\(99\)00066-4](https://doi.org/10.1016/S0037-0738(99)00066-4), 1999.
- Shao, L., Zhang, P., Hilton, J., Gayer, R., Wang, Y., Zhao, C., and Luo, Z.: Paleoenvironments and paleogeography of the Lower and lower Middle Jurassic coal measures in the Turpan-Hami oil-prone coal basin, northwestern China, *Am. Assoc. Petr. Geol. B.*, 87, 335–355, <https://doi.org/10.1306/09160200936>, 2003.
- Shen, C. B., Mei, L. F., Liu, L., Tang, J. G., and Zhou, F.: Evidence from apatite and zircon fission track analysis for Mesozoic–Cenozoic uplift thermal history of Bogeda Mountain of Xinjiang, Northwest China, *Mar. Geol. Quat. Geol.*, 87–92 (in Chinese with English abstract), 2006.
- Shen, T., Chen, Y., Wang, G., Ji, J., Wang, Y., Zhang, P., Sotiriou, P., Guo, R., and Xu, Z.: Detrital zircon geochronology analysis of the Late Mesozoic deposition in the Turpan-Hami basin: Implications for the uplift history of the Eastern Tian Shan, north-western China, *Terra Nova*, 32, 166–178, <https://doi.org/10.1111/ter.12445>, 2020.
- Shen, T., Ding, Y., Wang, G., Zhang, D., and Zhao, Z.: Quaternary deformation along the Gobi–Tian Shan fault in the easternmost Tian Shan (Harlik mountain), central Asia, *Remote Sens.*, 16, 3343, <https://doi.org/10.3390/rs16173343>, 2024.
- Smith, A. G. G., Fox, M., Schwanghart, W., and Carter, A.: Comparing methods for calculating channel steepness index, *Earth-Sci. Rev.*, 227, 103970, <https://doi.org/10.1016/j.earscirev.2022.103970>, 2022.
- Sobel, E. R., Oskin, M., Burbank, D., and Mikolaichuk, A.: Exhumation of basement-cored uplifts: Example of the Kyrgyz Range quantified with apatite fission track thermochronology, *Tectonics*, 25, 17, <https://doi.org/10.1029/2005tc001809>, 2006a.
- Sobel, E. R., Chen, J., and Heermance, R. V.: Late Oligocene–Early Miocene initiation of shortening in the Southwestern Chinese Tian Shan: Implications for Neogene shortening rate variations, *Earth Planet. Sc. Lett.*, 247, 70–81, <https://doi.org/10.1016/j.epsl.2006.03.048>, 2006b.
- Song, D. F., Glorie, S., Xiao, W. J., Collins, M. S., Gillespie, J., Jepson, G., and Li, Y. C.: Tectono-thermal evolution of the southwestern Alxa Tectonic Belt, NW China: Constrained by apatite U–Pb and fission track thermochronology, *Tectonophysics*, 722, 577–594, <https://doi.org/10.1016/j.tecto.2017.11.029>, 2018.
- Song, S. D., Li, J. A., Liu, X. Y., Wang, Y. D., Liang, W. T., and Yuan, S. H.: Mesozoic–Cenozoic exhumation history of the Bogda Range, Eastern Tianshan: Insights from apatite fission track thermochronology, *Minerals*, 13, 71, <https://doi.org/10.3390/min13010071>, 2023.
- Sui, Q.-L., Wang, Q., Zhu, D.-C., Zhao, Z.-D., Chen, Y., Santosh, M., Hu, Z.-C., Yuan, H.-L., and Mo, X.-X.: Compositional diversity of ca. 110 Ma magmatism in the northern Lhasa Terrane, Tibet: Implications for the magmatic origin and crustal growth in a continent–continent collision zone, *Lithos*, 168–169, 144–159, <https://doi.org/10.1016/j.lithos.2013.01.012>, 2013.
- Sun, J. B., Chen, W., Qin, K. Z., Danisik, M., Evans, N. J., McInnes, B. I. A., Shen, Z., Zhao, S. F., Zhang, B., Yin, J. Y., and Tao, N.: Mesozoic exhumation of the Jueluotage area, Eastern Tianshan, NW China: constraints from (U–Th)/He and fission-track thermochronology, *Geol. Mag.*, 158, 1960–1976, <https://doi.org/10.1017/s0016756821000522>, 2021.
- Sun, J. B., Sun, T. F., Chen, W., Yu, S., Yin, J. Y., Li, C., Zhang, Y., and Liu, X. Y.: Thermo-tectonic evolution history of Hongyuntan area, eastern Tianshan, Xinjiang: Constrained from Ar–Ar and (U–Th)/He dating, *Acta Petrol. Sin.*, 31, 3732–3742 (in Chinese with English abstract), 2015.
- Suo, Y. H., Li, S. Z., Cao, X. Z., Dong, H., Li, X. Y., and Wang, X. Y.: Two-stage eastward diachronous model of India–Eurasia collision: Constraints from the intraplate tectonic records in Northeast Indian Ocean, *Gondwana Res.*, 102, 372–384, <https://doi.org/10.1016/j.gr.2020.01.006>, 2022.
- Tang, W., Zhang, Z., Li, J., and Chen, C.: Geochemical characteristics and tectonic significance of the Cretaceous volcanic rocks in the Eastern Terminal of the Altyn Tagh fault zones, *Earth Sci. Front.*, 19, 51–62, 2012.
- Tang, W. H., Zhang, Z. C., Li, J. F., Li, K., Luo, Z. W., and Chen, Y.: Mesozoic and Cenozoic uplift and exhumation of the Bogda Mountain, NW China: Evidence from apatite fission track analysis, *Geosci. Front.*, 6, 617–625, <https://doi.org/10.1016/j.gsf.2014.04.006>, 2015.
- Tian, Z., Xiao, W., Zhang, Z., and Lin, X.: Fission-track constrains on superposed folding in the Beishan orogenic belt, southernmost Altai, *Geosci. Front.*, 7, 181–196, <https://doi.org/10.1016/j.gsf.2015.11.007>, 2016.

- van der Beek, P. A., Delvaux, D., Andriessen, P. A. M., and Levi, K. G.: Early Cretaceous denudation related to convergent tectonics in the Baikal region, SE Siberia, *J. Geol. Soc.*, 153, 515–523, <https://doi.org/10.1144/gsjgs.153.4.0515>, 1996.
- van der Beek, P., Van Melle, J., Guillot, S., Pêcher, A., Reiners, P. W., Nicolescu, S., and Latif, M.: Eocene Tibetan plateau remnants preserved in the northwest Himalaya, *Nat. Geosci.*, 2, 364–368, <https://doi.org/10.1038/ngeo503>, 2009.
- van Hinsbergen, D. J. J., Lippert, P. C., Dupont-Nivet, G., McQuarrie, N., Doubrovine, P. V., Spakman, W., and Torsvik, T. H.: Greater India Basin hypothesis and a two-stage Cenozoic collision between India and Asia, *Proc. Natl. Acad. Sci. USA*, 109, 7659–7664, <https://doi.org/10.1073/pnas.1117262109>, 2012.
- Vermeesch, P.: RadialPlotter: A Java application for fission track, luminescence and other radial plots, *Radiat. Meas.*, 44, 409–410, <https://doi.org/10.1016/j.radmeas.2009.05.003>, 2009.
- Vermeesch, P.: Statistics for LA-ICP-MS based fission track dating, *Chem. Geol.*, 456, 19–27, <https://doi.org/10.1016/j.chemgeo.2017.03.002>, 2017.
- Wang, F., Luo, M., He, Z., Wang, Y., Zheng, B., Zhang, Z., Hu, X., and Zhu, W.: Mid-Cretaceous accelerated cooling of the Beishan Orogen, NW China: Evidence from apatite fission track thermochronology, *Lithosphere*, 2023, lithosphere_2023_239, https://doi.org/10.2113/2023/lithosphere_2023_239, 2024.
- Wang, G., Cao, K., Zhang, K., Wang, A., Liu, C., Meng, Y., and Xu, Y.: Spatio-temporal framework of tectonic uplift stages of the Tibetan Plateau in Cenozoic, *Sci. China Earth Sci.*, 54, 29–44, <https://doi.org/10.1007/s11430-010-4110-0>, 2011.
- Wang, Q. C., Li, S. J., and Du, Z. L.: Differential uplift of the Chinese Tianshan since the Cretaceous: constraints from sedimentary petrography and apatite fission-track dating, *Int. J. Earth Sci.*, 98, 1341–1363, <https://doi.org/10.1007/s00531-009-0436-2>, 2009.
- Wang, T., Guo, L., Zhang, L., Yang, Q., Zhang, J., Tong, Y., and Ye, K.: Timing and evolution of Jurassic–Cretaceous granitoid magmatism in the Mongol–Okhotsk belt and adjacent areas, NE Asia: Implications for transition from contractional crustal thickening to extensional thinning and geodynamic settings, *J. Asian Earth Sci.*, 97, 365–392, <https://doi.org/10.1016/j.jseaes.2014.10.005>, 2015.
- Wang, T., Tong, Y., Xiao, W., Guo, L., Windley, B. F., Donskaya, T., Li, S., Tserendash, N., and Zhang, J.: Rollback, scissor-like closure of the Mongol–Okhotsk Ocean and formation of an orocline: magmatic migration based on a large archive of age data, *Natl. Sci. Rev.*, 9, nwab210, <https://doi.org/10.1093/nsr/nwab210>, 2022.
- Wang, X., Kellner, A. W. A., Jiang, S., Cheng, X., Wang, Q., Ma, Y., Paidoula, Y., Rodrigues, T., Chen, H., Sayão, J. M., Li, N., Zhang, J., Bantim, R. A. M., Meng, X., Zhang, X., Qiu, R., and Zhou, Z.: Egg accumulation with 3D embryos provides insight into the life history of a pterosaur, *Science*, 358, 1197–1201, <https://doi.org/10.1126/science.aan2329>, 2017.
- Wang, Y., Wang, Y., Yin, J., Thomson, S. N., Xiao, W., He, Z., Chen, W., Cai, K., Wu, M., and Meng, Y.: Mesozoic exhumation of the northern West Junggar, NW China: Insights from low-temperature thermochronometers, *Tectonophysics*, 862, 229939, <https://doi.org/10.1016/j.tecto.2023.229939>, 2023a.
- Wang, Y. N., Cai, K. D., Sun, M., Xiao, W. J., De Grave, J., Wan, B., and Bao, Z. H.: Tracking the multi-stage exhumation history of the western Chinese Tianshan by apatite fission track (AFT) dating: Implication for the preservation of epithermal deposits in the ancient orogenic belt, *Ore Geol. Rev.*, 100, 111–132, <https://doi.org/10.1016/j.oregeorev.2017.04.011>, 2018.
- Wang, Y. N., Zhang, J., Huang, X., and Wang, Z. J.: Cenozoic exhumation of the Tianshan as constrained by regional low-temperature thermochronology, *Earth-Sci. Rev.*, 237, 24, <https://doi.org/10.1016/j.earscirev.2023.104325>, 2023b.
- Whipple, K. X. and Tucker, G. E.: Dynamics of the stream-power river incision model: Implications for height limits of mountain ranges, landscape response timescales, and research needs, *J. Geophys. Res.*, 104, 17661–17674, <https://doi.org/10.1029/1999JB900120>, 1999.
- Whipple, K. X., DiBiase, R. A., Ouimet, W. B., and Forte, A. M.: Preservation or piracy: Diagnosing low-relief, high-elevation surface formation mechanisms, *Geology*, 45, 91–94, <https://doi.org/10.1130/G38490.1>, 2017.
- Windley, B. F., Allen, M. B., Zhang, C., Zhao, Z. Y., and Wang, G. R.: Paleozoic accretion and Cenozoic re-deformation of the Chinese Tien-Shan-Range, Central Asia, *Geology*, 18, 128–131, [https://doi.org/10.1130/0091-7613\(1990\)018<0128:Paacro>2.3.Co;2](https://doi.org/10.1130/0091-7613(1990)018<0128:Paacro>2.3.Co;2), 1990.
- Windley, B. F., Alexeiev, D., Xiao, W. J., Kroner, A., and Badarch, G.: Tectonic models for accretion of the Central Asian Orogenic Belt, *J. Geol. Soc.*, 164, 31–47, <https://doi.org/10.1144/0016-76492006-022>, 2007.
- Wobus, C., Whipple, K. X., Kirby, E., Snyder, N., Johnson, J., Spyropolou, K., Crosby, B., and Sheehan, D.: Tectonics from topography: Procedures, promise, and pitfalls, in: *Tectonics, Climate, and Landscape Evolution*, Geological Society of America, [https://doi.org/10.1130/2006.2398\(04\)](https://doi.org/10.1130/2006.2398(04)), 2006.
- Wu, H., Li, C., Hu, P., and Li, X.: Early Cretaceous (100–105 Ma) adakitic magmatism in the Dachagou area, northern Lhasa terrane, Tibet: implications for the Bangong–Nujiang Ocean subduction and slab break-off, *Int. Geol. Rev.*, 57, 1172–1188, <https://doi.org/10.1080/00206814.2014.886152>, 2015.
- Wu, M., Yin, J., He, Z., Xiao, W., Wang, Y., Chen, W., Wang, Y., Sun, J., Li, D., and Meng, Y.: Mesozoic thermo-tectonic evolution of the Western Altai Orogenic Belt (NW China): Insights from low-temperature thermochronology, *Lithosphere*, 2023, 8161000, <https://doi.org/10.2113/2023/8161000>, 2023.
- Xiang, D. F., Zhang, Z. Y., Xiao, W. J., Zhu, W. B., Zheng, D. W., Li, G. W., Zheng, B. H., Song, D. F., Han, C. M., and Pang, J. Z.: Episodic Meso-Cenozoic denudation of Chinese Tianshan: evidence from detrital apatite fission track and zircon U–Pb data, southern Junggar Basin margin, NW China, *J. Asian Earth Sci.*, 175, 199–212, <https://doi.org/10.1016/j.jseaes.2018.07.042>, 2019.
- Xiao, W. J., Zhang, L. C., Qin, K. Z., Sun, S., and Li, J. L.: Paleozoic accretionary and collisional tectonics of the Eastern Tianshan (China): Implications for the continental growth of Central Asia, *Am. J. Sci.*, 304, 370–395, <https://doi.org/10.2475/ajs.304.4.370>, 2004.
- Xiao, W. J., Windley, B. F., Allen, M. B., and Han, C. M.: Paleozoic multiple accretionary and collisional tectonics of the Chinese Tianshan orogenic collage, *Gondwana Res.*, 23, 1316–1341, <https://doi.org/10.1016/j.gr.2012.01.012>, 2013.

- Yang, R., Willett, S. D., and Goren, L.: In situ low-relief landscape formation as a result of river network disruption, *Nature*, 520, 526–529, <https://doi.org/10.1038/nature14354>, 2015a.
- Yang, Y. T., Guo, Z. X., Song, C. C., Li, X. B., and He, S.: A short-lived but significant Mongol-Okhotsk collisional orogeny in latest Jurassic-earliest Cretaceous, *Gondwana Res.*, 28, 1096–1116, <https://doi.org/10.1016/j.gr.2014.09.010>, 2015b.
- Yin, A. and Harrison, T. M.: Geologic Evolution of the Himalayan-Tibetan Orogen, *Annu. Rev. Earth Pl. Sc.*, 28, 211–280, <https://doi.org/10.1146/annurev.earth.28.1.211>, 2000.
- Yin, J. Y., Chen, W., Hodges, K. V., Xiao, W. J., Cai, K. D., Yuan, C., Sun, M., Liu, L. P., and van Soest, M. C.: The thermal evolution of Chinese central Tianshan and its implications: Insights from multi-method chronometry, *Tectonophysics*, 722, 536–548, <https://doi.org/10.1016/j.tecto.2017.11.037>, 2018.
- Yuan, J., Yang, Z., Deng, C., Krijgsman, W., Hu, X., Li, S., Shen, Z., Qin, H., An, W., He, H., Ding, L., Guo, Z., and Zhu, R.: Rapid drift of the Tethyan Himalaya terrane before two-stage India-Asia collision, *Natl. Sci. Rev.*, 8, nwaa173, <https://doi.org/10.1093/nsr/nwaa173>, 2021.
- Zaprowski, B. J., Pazzaglia, F. J., and Evenson, E. B.: Climatic influences on profile concavity and river incision, *J. Geophys. Res.*, 110, 2004JF000138, <https://doi.org/10.1029/2004JF000138>, 2005.
- Zhang, B., Yang, J., Yang, L., Chen, H., Liu, J., Wang, F., and Wu, L.: Mesozoic–Cenozoic exhumation processes of the Harlik Mountain (East Tianshan), NW China: Evidence from apatite (U–Th)/He thermochronology, *Lithosphere*, 2023, lithosphere_2023_210, https://doi.org/10.2113/2023/lithosphere_2023_210, 2023.
- Zhang, D., Wang, G., Pullen, A., Abell, J. T., Cheng, F., Shen, T., Ji, J., and Zhang, M.: A westerly dominated Early Cretaceous aeolian system in the Hami Basin, NW China, *Geol. Soc. Am. Bull.*, 137, 137–155, <https://doi.org/10.1130/B37436.1>, 2024.
- Zhang, K.-J.: Genesis of the Late Mesozoic Great Xing’an Range Large Igneous Province in eastern central Asia: A Mongol–Okhotsk slab window model, *Int. Geol. Rev.*, 56, 1557–1583, <https://doi.org/10.1080/00206814.2014.946541>, 2014.
- Zhang, K.-J., Yan, L.-L., and Ji, C.: Switch of NE Asia from extension to contraction at the mid-Cretaceous: A tale of the Okhotsk oceanic plateau from initiation by the Perm Anomaly to extrusion in the Mongol–Okhotsk ocean?, *Earth-Sci. Rev.*, 198, 102941, <https://doi.org/10.1016/j.earscirev.2019.102941>, 2019.
- Zhang, W., Chen, W., Sun, J. B., Shen, Z., and Zhang, Y.: Thermal history and exhumation processes in the Chinese South Tianshan: constraints from Ar-40/Ar-39 and (U–Th)/He ages, *Int. J. Earth Sci.*, 110, 1575–1592, <https://doi.org/10.1007/s00531-021-02031-x>, 2021.
- Zhang, Z. Y., Zhu, W. B., Shu, L. S., Wan, J. L., Yang, W., Su, J. B., and Zheng, B. H.: Apatite fission track thermochronology of the Precambrian Aksu blueschist, NW China: Implications for thermo-tectonic evolution of the north Tarim basement, *Gondwana Res.*, 16, 182–188, <https://doi.org/10.1016/j.gr.2009.04.006>, 2009.
- Zhang, Z. Y., Zhu, W. B., Shu, L. S., Wan, J. L., Yang, W., Zheng, B. H., and Su, J. B.: Multi-stage exhumation of the NE Tarim Precambrian bedrock, NW China: constraints from apatite fission track thermochronology in the Kuluketage area, *Terra Nova*, 23, 324–332, <https://doi.org/10.1111/j.1365-3121.2011.01017.x>, 2011.
- Zhang, Z. Y., Zhu, W. B., Zheng, D. W., Zheng, B. H., and Yang, W.: Apatite fission track thermochronology in the Kuluketage and Aksu areas, NW China: Implication for tectonic evolution of the northern Tarim, *Geosci. Front.*, 7, 171–180, <https://doi.org/10.1016/j.gsf.2015.08.007>, 2016.
- Zheng, D., Chang, S.-C., Ramezani, J., Xu, X., Xu, H., Wang, H., Pei, R., Fang, Y., Wang, J., Wang, B., and Zhang, H.: Calibrating the Early Cretaceous Urho Pterosaur fauna in Junggar Basin and implications for the evolution of the Jehol Biota, *Geol. Soc. Am. Bull.*, 136, 765–773, <https://doi.org/10.1130/B36795.1>, 2023.
- Zhimulev, F. I., Vetrov, E. V., Novikov, I. S., Van Ranst, G., Nachtergaele, S., Dokashenko, S. A., and De Grave, J.: Mesozoic intracontinental orogeny in the tectonic history of the Kolyvan’–Tomsk Folded Zone (Southern Siberia): a synthesis of geological data and results of apatite fission track analysis, *Russ. Geol. Geophys.*, 62, 1006–1020, <https://doi.org/10.2113/rgg20204172>, 2021.
- Zhu, W., Shu, L., Wan, J., Sun, Y., Wang, F., and Zhao, Z.: Fission-track evidence for the exhumation history of Bogda-Harlik Mountains, Xinjiang since the Cretaceous, *Acta Geol. Sin.*, 16–22 (in Chinese with English abstract), 2006.
- Zhu, W. B., Wan, J. L., Shu, L. S., Sun, Y., and Wang, F.: Mesozoic–Cenozoic thermal history of Turpan–Hami basin: evidence from apatite fission track, *Progr. Natural.*, 14, 1194–1198 (in Chinese with English abstract), <https://doi.org/10.3321/j.issn:1002-008X.2004.10.017>, 2004.
- Zhu, W. B., Zhang, Z., Shu, L., Wan, J., Lu, H., Wang, S., Yang, W., and Su, J.: Uplift and exhumation history of the Precambrian basement, Northern Tarim: Evidence from apatite fission track data, *Acta Petrol. Sin.*, 23, 1671–1682 (in Chinese with English abstract), <https://doi.org/10.3969/j.issn.1000-0569.2007.07.013>, 2007.